

Graduate Laboratory Report

CONSTRUCTION AND TESTING OF A 20.1 MHz DIPOLE ARRAY

E. Araya, A. Datta, & Urvashi R. V.

*Physics Department, New Mexico Institute of Mining
and Technology, Socorro, NM 87801*

ABSTRACT

This report describes the design, construction and testing of a 20.1 MHz dipole radio telescope. Two 2-element dipole arrays were built for the detection of 20.1MHz radio emission from the Jupiter-Io interaction, strong solar bursts, the galactic background and the transit of the galactic center. We followed the design used in the NASA Radio Jove project (<http://radiojove.gsfc.nasa.gov>), to construct the dipole array. We characterized and tested the receivers, and conducted observations at two sites: the Etscorn Campus Observatory, and Workman Center. We observed almost continuously during 27 days at the Etscorn site, and during approximately 20 days at the Workman site. We detected a variety of RFI signals. In both sites RFI occurred more often during the day time, as expected by human activity. The RFI environment at the Workman Center site is worse than the one at the Etscorn Observatory, nevertheless, both sites present substantial RFI confusion problems and thus are far from optimal to conduct low frequency radio observations. No confirmed Jovian bursts were detected during our observations. We have outlined a possible undergraduate laboratory experiment that can use this equipment to understand the basics of instrumentation in radio astronomy.

We would like to thank Dr.Dave Westpfahl for providing the funds to purchase two Radio Jove antenna and receiver kits, and for the use of laboratory equipment for the construction of the antennas and receivers.

Contents

1	20.1 MHZ RADIO SOURCES	3
1.1	Diffuse Galactic Radio Noise	3
1.2	Solar Decameter Emission	3
1.3	Jovian Decametric Emission	6
2	CONSTRUCTION OF THE 20.1 MHZ DIPOLE RADIO TELESCOPE	9
2.1	Half-wave Horizontal Dipole Antenna Array	9
2.2	20.1 MHz Radio Receiver	12
3	TESTING AND CHARACTERIZATION	15
4	OBSERVATIONS	18
4.1	Etscorn Observations	18
4.2	Workman Center Observations	18
5	RESULTS AND DISCUSSION	18
5.1	Radio Interference	19
5.2	Possible Detection of the Sun	19
6	POTENTIAL USE OF THE DIPOLE ARRAY FOR A STUDENT LAB- ORATORY	20
7	SUMMARY	22
A	Dipole antenna (array) radiation patterns	23
B	Python Program to Convert Data from SPD to ASCII Format	27
C	Data Recording/Handling Software for Linux.	30

1. 20.1 MHZ RADIO SOURCES

1.1. Diffuse Galactic Radio Noise

While observing any radio loud object in the sky, the instrument records a steady signal, which increases the base level of the received signal. This is due to the radio noise from the electrons gyrating in the magnetic field of our Galaxy¹.

Characteristics and Mechanism

In addition to discrete sources and line emission of our Galaxy, there is a Galactic background radiation. This continuous distribution of diffuse radiation is manifested by the narrow ridge extending all around the Galactic plane. Away from the Galactic plane the radiation falls off far more rapidly than it does in the Galactic plane.

The Galactic background is composed of two principal components: one concentrated close to the Galactic plane with a thermal spectrum and the other having a maximum along the Galactic plane, but of greater extent away from the plane, with a non-thermal spectrum. While the thermal component arises from ionized hydrogen, the non-thermal one is due to the synchrotron radiation from relativistic electron moving in the Galactic magnetic field.

The linear polarization of the Galactic background radiation confirms the mechanism to be synchrotron emission. The equivalent temperature of the synchrotron emission depends both on the density of the relativistic electron and the magnetic field strength. If the electron density were constant, the temperature distribution can give the magnetic field distribution across the Galactic background.

1.2. Solar Decameter Emission

The Sun is an extremely complex radio source. Its radio emission has structure on angular scales $< 1''$ to more than 0.5° . Furthermore, the intrinsic brightness distribution varies on timescales ranging from less than one second, to minutes, hours, days, and years. Additional problems are introduced by the Sun's (differential) rotation.

Characteristics of Solar Bursts

The radio emission from the Sun has three distinct components: originating from quiet Sun, from bright regions, and from transient disturbances such as flares.

¹ Kraus J.D. *Radio Astronomy* and <http://ufro1.astro.ufl.edu>

- The quiet Sun component is thermal radio emission from the solar atmosphere.
- Radio emission from bright regions correspond to slowly varying radiation also due to thermal emission.
- The third component consists of radio bursts. These are generally associated with the solar flares and originate from all levels of the solar atmosphere, between the lower chromosphere (millimeter and centimeter waves) and outer corona to heights of several solar radii (meter and decameter waves). These radio bursts can occur between 4 mm to 40 m wavelengths.

The centimeter wave bursts are the simplest and are characterized by a rapid rise in intensity, usually followed by a slower decline. The radiation is partially circularly polarized and mostly a smooth continuum. They can be subdivided into impulsive bursts (lasting few minutes), post-bursts (lasting few tens of a minutes) and gradual rise and fall of intensity (lasts few tens of a minute). The decimeter wave bursts are more complex, showing a great variety of fluctuations superimposed upon the continuum².

The decameter and meter wave bursts have great variety and complexity. These solar radio bursts are classified on the basis of their temporal and spectral characteristics as follows:

- Type I :- Short, narrow band (~ 5 MHz) events that usually occur in great numbers together with a broader band continuum. May last for hours or days. The radiation is strongly circularly polarized and occurs in association with the appearance of visible active regions on the solar disk.
- Type II :- Slow drift from high to low frequencies (20 MHz to 1 MHz per second). Often show fundamental and second harmonic frequency structure.
- Type III :- Rapidly drift from high to low frequencies (20 MHz to 1 MHz per second). May exhibit harmonics. Often accompany the flash phase of large flares.
- Type IV :- Flare-related broad-band continua. It is partially polarized, smooth continuum emission, occurring over a very wide range of frequencies between centimeter and decameter waves and lasting for about 10 minutes to a few hours.
- Type V :- Broad-band continua which may appear with III bursts. Lasts from few seconds to a few minutes, with duration increasing as frequency decreases and mostly limited to meter waves.

²Kundu M. *Solar Radiation*

Detection by Ionospheric Effects:

With large solar flares come blasts of x-rays. When the x-rays hit the Earth's ionosphere, the way the ionosphere reflects radio waves is disturbed. At short wave frequencies, a dip in signal strength of distant stations can often be observed. At VLF frequencies, below 150 kHz, the opposite effect is observed and the signal strength of distant station will jump suddenly and slowly decline. Using a VLF receiver permanently tuned to a distant station or even to static from distant tropical rain storms is considered a quite reliable way to detect x-ray solar flares.

Magnetic Storms :

Solar flares also emit high velocity charged particles. These particles take one or two days to reach Earth, (where as the radio waves and x-rays reach us in about 9 minutes). When the particles arrive they slam into the Earth's magnetic field and distort it. Some of the particles are channeled along the magnetic field lines towards the poles and produce auroras. The distortion of the magnetic field are the geomagnetic storms. These storms can be observed with magnetometers. Severe geomagnetic storms can disrupt large electric power grids and even cause blackouts.

Thermal Emissions :

Everything emits electromagnetic waves due to thermal emission. The Sun is about 6000 K at the photosphere. The "quiet Sun", that is, the Sun when it is in a period of low sunspot activity, is easily detected at microwave frequencies where its thermal emission is strongest.

How to observe?

Using a 20.1 MHz receiver and a dipole antenna, one can detect strong Solar bursts. If the receiver is run over the noon hour, the strip chart will show more bumps and spikes than that in night. This is due to the active ionosphere in the day³. Solar bursts are in general stronger than Jovian bursts (see below), thus they are easier to detect. In the strip chart recording, the solar flares would be apparent from a steep rise and fall of the radio signal within a fraction of a minute.

After a burst candidate has been located in the data, it can be verified as a real burst by comparing it with data from different solar observatories, which have real time data available online.

³Richard S. Flagg, *Listening to Jupiter* and <http://www.radiosky.com>

1.3. Jovian Decametric Emission

The Jovian decametric emission was discovered in 1955 by B.F. Burke and K.L. Franklin at 22.2 MHz. The emission has an upper cutoff frequency of ~ 39.5 MHz. It can be detected from ground based stations from the upper cutoff frequency of the emission down to the cutoff frequency of the terrestrial ionosphere which is usually around 5 to 10 MHz. The peak of the intensity of the emission occurs at around 8 MHz.

Physics behind Jovian Emission

If charged particles (i.e., electrons or protons) move in a magnetic field \vec{B} and the velocity \vec{v} is perpendicular to \vec{B} , the electron starts to move in a circle (gyration). If the \vec{v} is not entirely perpendicular to the magnetic field, it starts to move in a spiral.

Billions of electrons spiraling along Jupiter’s magnetic field lines radiate electro-magnetic waves from 1 – 40 MHz (see Figure 1). Spiraling electrons radiate right-circularly-polarized (RCP) electro-magnetic waves at or near the local gyrofrequency $\omega_g = 2.8 \times B_g [\text{MHz}]$, where B_g is the local magnetic field. Since the emitted frequency depends on the local magnetic field strength, the emissions from other planets (e.g., Saturn, Uranus, Neptune) having lower magnetic fields, are lower in frequency ($< 2 \text{ MHz}$) and are not detectable on the surface of Earth due to ionospheric cut-off.

Electrons are accelerated up to a few keV (or more) at Io by Alfvén waves generated by Io’s movement through the Jovian magnetic field. Those electrons travel in spirals to Jupiter on magnetic field lines. As Jupiter’s magnetic field increases, the frequency of the emitted electro-magnetic waves also increases. The mechanism responsible for the emission is believed to be the cyclotron maser instability. The emission is beamed into a thin hollow cone with axis parallel to the direction of the magnetic field lines in the region where the emission originates (near the Jovian magnetic poles). The opening angle of the hollow cone seems to be around 70 to 80 degrees. The radio waves are emitted in thin hollow cones with axis parallel to the magnetic field line. The emission can only be detected at Earth if the thin walls of the cone intersect the direction of Earth. The Io-related emission is emitted from a Previously Energized Flux Tube (PEFT), which is 20 to 0 degrees behind the current Io Flux Tube (IFT). These Alfvén waves produce an electric field parallel to the magnetic field, which accelerates the electrons towards Jupiter⁴. The emissions are produced by electrons ascending the Io magnetic flux tube after having mirrored near the top of the Jovian ionosphere. So the emission occur at a frequency slightly above the local gyrofrequency.

⁴<http://www.jupiterradio.com/jove-emission.php>

Characteristics of Emission - Spectra

Most of the radio waves from Jupiter are polarized. In fact, the polarization of the radio emission from Jupiter indicated the existence of a magnetic field in that planet. The decametric emission occur in episodes called "storms", lasting from a few minutes to several hours. Two distinctive types of bursts can be received during a storm. The Long Bursts vary slowly in intensity with time and last from a few seconds to several tens of seconds, having an instantaneous bandwidth of a few MHz. The Short bursts are very short in duration, have instantaneous bandwidth of a few kHz to a few tens of kHz, and drift downward in frequency at a rate of typically 20 MHz/s. They arrive at a rate of a few to several hundred bursts per second. In a 5 kHz bandwidth receiver they last only a few milliseconds. Sometimes both types of bursts can be detected simultaneously.

The probabilities of detecting the emission depend strongly on the values of the Jovian central meridian longitude (CML), the Io Phase, and the Jovicentric declination of the Earth (DE). The CML is the value of the System III longitude of Jupiter facing the Earth. The Io Phase is the angle of Io with respect to superior geocentric conjunction.

Table 1: Jovian Radio Bursts

Io-related storms	Characteristics
Io-A	Right Hand Polarized and mostly long bursts
Io-B	Right Hand Polarized and mostly short bursts
Io-C	Left Hand Polarized, long and short bursts

How to observe?

The best time to conduct low frequency radio observations of Jupiter is at night, between 10 PM and 7 AM local time when the ionosphere is more transparent for low frequency signals and there are less RFI from nearby radio stations. The probabilities of detecting the emission are higher during Io-related storm periods. Data should be recorded during the time when Jupiter is inside the beam of the antenna⁵.

Jovian radio burst are always detectable above the galactic-background noise. Different properties of the Jovian noise makes it identifiable above the constant 'hiss' of the galactic-background noise. Long and Short bursts also have other identifying features. Generally the emissions extend over at least several hundred kHz. The storm will often begin with a few weak noise bursts. As the storm increases it becomes more easier to identify. Intense bursts

⁵<http://ufro1.astro.ufl.edu>

may last for tens of seconds and then subside. After several seconds or even a few minutes the activity may resume.

Several types of interference are commonly detected during an observation. The following is a short list and description of some of the common types :

- Stations : There are many types of stations, voice, telegraphic (Morse code), telex, sweeper (some are ionospheric sounding stations), CW or continuous wave (no modulation). Stations are narrow band; usually they disappear if one tunes a few kHz away.
- Lightning crashes: Local lightning crashes are usually strong. They last for a second or less. Under some circumstances the ionosphere may reflect distant lightning crashes. They are usually weaker and occasionally they may look like S bursts. Lightning crashes are wide band; they don't disappear by tuning the receiver to a different frequency.
- Buzz: It originates in coronal discharges from power lines and insulators. It is wide band and can be easily identified by its characteristic 120 Hz.
- Pops: Usually generated from power line transient. They are the result of the sudden connection or disconnection of electric appliances and electric motors. Common sources of pops are water pumps, air conditioners, and refrigerators.

2. CONSTRUCTION OF THE 20.1 MHz DIPOLE RADIO TELESCOPE

2.1. Half-wave Horizontal Dipole Antenna Array

Dipole Antenna Radiation Pattern

The radiation pattern of a single center-fed half-wave dipole in free space can be computed by modeling the dipole current density, and computing the corresponding electric and magnetic fields and the power radiated per solid angle. In the presence of a perfectly conducting ground plane, the radiation pattern can be computed using the method of images where the resultant beam arises from the coherent superposition of the radiation pattern amplitudes of the dipole and its image. The radiation pattern of a two element dipole array can be computed by the coherent superposition of the radiation pattern amplitudes of two dipoles and their images.

The gain and directivity of a two element dipole array, can be controlled by varying the height of the dipoles from the ground, the spacing between the two dipoles in the array (baseline), and the phase difference between the two dipoles (via a phasing cable or electronic steering).

Appendix A describes the calculation of antenna radiation patterns for (i) a single half-wave center-fed linear dipole in free space (Figure 2), (ii) a single half-wave dipole above an infinitely large flat conductor (figures 3, 4), and (iii) two half-wave dipoles placed a certain distance apart, both at a fixed height from the ground (a two element array) (see Figures 5, 6, 7).

Construction of a Single Jove Half-wave Dipole Antenna ⁶

Each Jove half-wave dipole antenna was constructed with the following specifications. (See Figure 8).

1. **Dipole length** : An operating frequency of 20.1 MHz was obtained with a linear center-fed half-wave dipole of total length calculated as follows.

Free Space Wavelength : $\lambda_m = 300/F_{MHz}$ or ($\lambda_{ft} = 984.17/F_{MHz}$)

So $\lambda_m/2 = 140/20.1 = 7.46m$ or ($\lambda_{ft}/2 = 492.08/20.1 = 24.48ft$)

This is true only for an infinitely thin dipole, and the following correction must be applied for a dipole of finite thickness.

⁶Ref: Jove RJ1.2 Antenna Manual, Dec 2004

$(\lambda/2)_{finite_thickness} = (\lambda/2)_{zero_thickness} * 0.95$ for the copper wire used as our dipole. Therefore, $\lambda_m/2 = 7.46 * 0.95 = 7.087m$ or $\lambda_m/2 = 24.48 * 0.95 = 23.26ft$. Our dipoles were cut to 7.09m (23.26ft) from tip to tip.

2. **Dipole height from ground** : The directivity of the antenna beam depends on the distance between the dipole and its image, which is twice the height of the dipole from the ground. Therefore the shape of the beam, and the direction of maximum gain of the antenna depends on the height. The height of the dipole from the ground was chosen so that the direction of maximum gain coincided with the elevation of Jupiter at transit. For an elevation of 42 degrees, the optimal height was around 15 ft. See figures 3 and 4.
3. **Antenna structure** : The dipole was constructed out of two pieces of copper wire each 11.63ft (3.5m) long, connected via a plastic insulator to each other. The two ends were then connected to support masts via ceramic insulators. The support masts were constructed out of pvc pipes that fit into each other to allow height adjustments, and were secured in place with bolts to fix the pipes at a fixed total length. Ground supports and ropes were used to secure the masts in a vertical position (despite the Socorro wind!)
4. **Co-axial transmission cable** : A RG-59/U co-axial cable was used to transfer the signal from the center of the antenna to the receiver. At the dipole end, one half of the dipole wire was connected to the core of the co-axial cable, and the other half to the braid of the coaxial cable. At 20.1MHz, the RG-59/U cable has a loss of 1.5dB per 100 ft (one fourth of the power is lost over a distance of 100 ft). Also, the RG-59/U has a velocity factor of 0.66 meaning that the signal travels at a speed of 0.66c through the cable. Therefore a free space wavelength of 48.955 ft for 20.1MHz corresponds to a wavelength of 32.31 ft within the cable. The chosen cable length was 1.5λ from the dipole to the receiver. The resulting cable length of 14.8m (48.3ft) corresponds to an attenuation of 12% of the input power (1.5 dB over 100 ft \rightarrow power reduces by 50% in 200ft \rightarrow power reduces by 12% in 48.3 ft).
5. **Impedance matching** : The feed impedance of a center fed half-wave dipole antenna in free space is approximately 73 ohms⁷. The RG-59/U coaxial cable has an impedance of 75 ohms. Approximate impedance matching is therefore directly achieved.

⁷Ref. <http://www.radio-electronics.com/info/antennas/dipole/dipole.php>

Jove Dipole Array⁸

Two half-wave dipole antennas were constructed and combined to produce a N–S dipole array with the antenna wires in the E–W direction. This allowed the gain to be doubled and required the formation and steering of a combined beam towards Jupiter’s location for maximum gain. The antenna wires were arranged parallel a distance of 25 ft from each other. This baseline length of $\lambda/2$ ensures that only the lowest frequency interference fringe modulates the beam of a single dipole. Increasing the baseline further will introduce multiple sidelobes. See figures 9 and 6.

Since the dipoles are fixed to the ground in the E–W direction, their individual beam patterns are fixed with maximum gain in the N–S direction in the form of one North pointing lobe, and one South pointing lobe. (See figure 5). Recall that the shape of the individual lobes and direction of maximum gain depend on the height of the dipoles from the ground, and have been optimized at 15ft for a 40 degree elevation.

The combination of the outputs of the two dipoles via a phasing cable (and power combiner), preferentially amplifies one lobe in the direction of the antenna connected to the shorter cable. (See figure 9). The choice of length of the phasing cable, and the antenna to whose output it must be connected is determined by the direction and elevation of Jupiter in the sky at transit (as it passes across the local meridian).

There are two factors that determine Jupiter’s position in the sky.

1. Jupiter’s declination in the sky follows a sinusoidal pattern with a period of 12 years. Between 2005 and 2010, it reaches it’s maximum southern declination, and in 2006 is between 10 and 20 degrees South of the Celestial equator.
2. The elevation of a source at a certain declination depends on the latitude of the observation site. From Socorro (34N), for 2006, Jupiter’s elevation at transit is about 42 degrees.

For a fixed baseline length, the beam of the dipole array can be steered along the elevation axis in two ways to point at Jupiter’s position in the sky.

1. Vary the length of the phasing cable to point at different elevations. Zero length phasing cable implies pointing vertically up, which given the radiation pattern of a dipole near

⁸Ref: Jove RJ1.2 Antenna Manual, Dec 2004

the ground corresponds to almost zero gain. Jupiter’s location at 42 degrees elevation at transit requires that a a delay cable be connected to the North dipole to steer the beam towards the Southern sky. Since the dipole heights are already optimized for maximum gain at 40 degrees elevation, steering the beam in the same direction will give maximum combined gain. The length of the phasing cable was chosen to be 0.375λ corresponding to a phase delay of 135 degrees to compensate for dipoles placed 25ft apart. See figure 5. ($\lambda = 48.955$ in free space. For a source at 42 degrees elevation, delay in free space = $25 \times \cos(42) = 18.579$ ft. The equivalent delay length in the RG-59/U cable is $18.579 \times 0.66 = 12.262$ ft = 0.379λ).

2. Since the dipole antenna radiation pattern is about 30 degrees wide, accurate pointing is not required, and additional elevation ranges (between 20 and 60 degrees) can be obtained just by changing the height of the dipoles from the ground, while using the fixed length of phasing cable. Over the next few years (2006 to 2010), the elevation of Jupiter varies between 30 and 50 degrees in elevation, and this same set-up can be easily re-used by changing the height of the dipoles between 10ft and 20ft.

This set-up of the antennas constituted a two element dipole array. The coaxial outputs from both antennas (feeds) were combined via a power combiner that adds up the signals now in phase, and transmits it to the receiver.

The antennas were put up on the Workman building roof with movable antenna supports and were also tested at the Etscorn Observatory. We constructed two such two-element dipole arrays, with the aim of combining the two dipole pairs in phase to increase signal to noise ratio. The combination can be done via another phasing cable of fixed length, or by electronic steering via software. Since we had already used a fixed phasing cable length for each dipole pair, it is more convenient to combine the two two-element arrays digitally.

2.2. 20.1 MHz Radio Receiver

Receiver Basics⁹

A heterodyne receiver works on the principle of combining an incoming signal with another produced by a local oscillator and using a low-pass filter to extract the lower beat frequency. This effectively steps the incoming signal down in frequency. The Jove receiver

⁹Ref: Jove RJ1.1 Receiver Kit Assembly Manual

converts MHz frequencies down to audio (kHz) frequencies (radio receiver) to allow direct connection to a speaker system, and digitization via off-the shelf PC audio cards.

The following are the various stages¹⁰ of signal propagation through the system (see Figure 10).

1. **Antenna** : As a 20.1 MHz (RF) EM wave strikes the dipole, the oscillating E-field components in the direction of the wire (parallel polarization) produces an oscillating voltage difference between the two halves of the dipole, and therefore also between the inner and outer wires of the co-axial cable, resulting in an AC current at the RF frequency.
2. **RF bandpass filter and preamplifier** : The signal from the antenna is first filtered to reject strong out of band interference, and then amplified by a factor of 10 by a JFET. The receiver input circuit was designed to efficiently transfer power from the antenna to the receiver while developing a minimum of noise within the receiver itself.
3. **Local Oscillator and Mixer** : The local oscillator generates a sinusoidal voltage waveform at a frequency near that of the incoming RF signal, and passes it to the mixer. The LO setting is chosen via a user controlled tuning knob. The mixer multiplies the LO signal with the incoming RF signal, to produce a new signal comprising of frequencies equal to the sum and difference of the two input frequencies. A low pass filter at this stage preserves only the part of the signal with frequency equal to the difference between the LO and the incoming RF frequency. For example, if the incoming signal is at 20.101 MHz, and the LO is tuned to 20.100 MHz, the resulting signal is at $0.001\text{MHz} = 1\text{kHz}$. This LO/mixer setup therefore converts 20MHz signals into audio frequency signals.
4. **Low Pass Filter** : To eliminate interfering radio stations at nearby frequencies, a filter with a pass-band only a few kHz wide is used on the audio frequency signal. Low audio frequencies of upto about 3.5kHz are passed, and higher frequencies are attenuated.
5. **Audio amplifiers** : The weak audio signal from the mixer is then amplified externally to drive a speaker assembly, and/or to serve as input to the microphone jack of a standard PC, to be recorded as sound.

¹⁰Ref: Jove RJ1.1 Receiver Kit Assembly Manual

Circuit Diagram of a 20.1 MHz Receiver

The schematic circuit diagram of the Jove receiver is shown in figure 11. (The following description is directly quoted from pages 8,9 of the Receiver Manual)

The signal from the antenna connector (J2) is coupled to a resonant circuit (bandpass filter L1,C2,C3) and then to the J310 transistor (Q1) where it is amplified. The output of the J-310 goes through another resonant filter (L3,C6) before being applied to the resonant input circuit (L4,C9,C10) of the SA602 integrated circuit(IC1), which serves as the local oscillator and the mixer. The center frequency of the LO is set by inductor L5 and adjusted by the tuning control R7. The audio output from IC1 passes through the low-pass audio filter (L6,L7,C20,C21, and C22). The audio signal is next amplified by IC2 (an NTE824) before going to the volume control R15. The final audio amplifier stages comprise IC3 (another NTE824), and the output transistors Q2(2n-3904) and Q3(2N-3906). The variable capacitors C2 and C6 and variable inductors L4 and L5 are for the purpose of tuning the receiver for operation at 20.1MHz.

The various components were received along with the radio Jove kit, and were first individually identified and checked with the listed list of parts. The components were then soldered onto the provided PCB and other connections made. The testing and characterization of the receiver is described in the section 3. Two such receivers were constructed, for the two phased dipole antenna pairs.

Data Acquisition Software

Data recorder for one receiver (on Linux or Windows)

The Jove receiver kit contained SkyPipe, a Windows based software for data recording. It records single channel microphone input power levels (with a 16 kHz sampling rate, and integration time of 0.1 s), and stores it on disk in the SPD sound file format. However, the 'free' version of the software neither allows direct access to the numbers, nor does it compute a dynamic spectrum.

A Linux based data recorder was written as a part of this project to gain access to the input voltages read directly from the audio device. The advantage was the ability to perform Fourier transforms on the signal to create and record dynamic spectra.

Appendix A lists the python scripts used to create a simple multi-threaded data recorder.

1. One thread samples the sound card input at a rate of 8 kHz (or 8000 samples per second). Every 0.1 seconds, the accumulated 800 samples are sent via a pipe to the second thread, where an 800 point FFT is performed.

2. Every 0.1 s, the spectrum resulting from each 800 point FFT is smoothed by a factor of 2, and written to disk to form the dynamic spectrum. The recorded frequency range is between 0 and 8 kHz and directly corresponds to the kHz difference in frequency between the RF signal detected by the antenna and that of the LO. (Also note that the audio low-pass filter attenuates frequencies above about 3.5 kHz). The total power for each 0.1 second integration is also recorded along with a time-stamp. The recorded values are at an arbitrary scale, depending on the currently set microphone gain on the machine used as the recorder. The FFT processing time for 800 samples is much less than the 0.1 seconds it takes to accumulate the samples, and so the data recording can proceed in real time without "clogging the pipe".
3. Additional functions are provided for data visualization of the power as a time series, along with the corresponding dynamic spectrum. A sample plot is shown in figure 12.

Appendix B lists python scripts to convert the Windows SkyPipe ".spd" files into ASCII format (for ease of plotting).

Data recorder for two receivers (on Linux)

To allow for the simultaneous recording of data from both dipole arrays (two separate receivers), a stereo signal was created with the two signals as the left and right channels. This was done by attaching connectors to the two ear-bud ends of a set of head-phone wires, and connecting each to a receiver. The input stereo microphone signal was then read via the python mixer module to separate the left and right channels which were recorded separately with the same time-stamps.

Electronic steering of a combined beam can then be done by adding the recorded voltage patterns with a phase shift corresponding to the distance between the two dipole arrays. We are still in the process of completing this.

3. TESTING AND CHARACTERIZATION

Testing and characterization of the receiver and dipoles were conducted during the first days of continuous observations at the Etscorn Observatory (see section 4). Further tests were done during the observations carried out at the Workman Center. The first test was to check the change in noise and baseline levels using only the receiver, connecting one dipole, and connecting both dipoles to the receiver. We expected that the receiver noise would be far less than the noise detected when the dipoles were plugged into the receiver because at

20 MHz the available electronics is known to have significant less noise than natural sources. In addition, we expected to see an increase in the baseline level when the dipoles were connected to the receiver.

Figure 13 shows the results of our test. The figure shows the counts obtained when both dipoles were connected to the receiver, when only one was plugged-in, and the receiver noise. As expected, the receiver noise is far less than the noise detected when the dipoles are connected. In addition, we detected an increase in the baseline level when one and two dipoles are used for the observations. This test showed that the receiver and dipoles were working as expected.

To further test and characterized the receiver and dipoles we used a 20 MHz signal generator. With the signal generator we conducted three experiments: 1. test the response of the dipoles and receiver to an artificially generated signal, 2. measure the bandwidth of the receiver, 3. find the approximate central frequency of the receiver bandpass at different positions of the tuning-knob.

1. Response of the Receiver to an Artificially Generated Signal: The goal of this experiment was to verify that the receiver was able to detect a test radio signal at ~ 20 MHz. To conduct this experiment we connected the signal generator to one of the dipoles and the other dipole was connected to the receiver. Then, we increased the amplitude of the signal generator output in steps of one Volt from 0 V to 9 V, and recored the response of the receiver. In Figure 14 we show the results of this experiment. We started with the dipole disconnected from the receiver to check the receiver noise, then we connected the dipole. We subsequently increased the amplitude of the signal produced by the signal generator as explicitly shown in the figure. This experiment shows that the dipoles and receiver were successfully working, i.e., we detected a clear increase of the baseline when more intense radiation from the signal generator was transmitted. One curious phenomenon observed in Figure 14 is an apparent saturation of the received signal at about 6000 counts, i.e., although we kept increasing the signal after 3 volts, no increase in the baseline level was detected. Given that we detected signals stronger than 6000 counts (see section 4), we conclude that this apparent saturation is caused by the signal generator and not by the receiver, that is, a changed in the amplitude voltage did not linearly changed the amplitude of the transmitted signal. Nevertheless, this non-linear behavior of the signal generator does not affect our conclusion that the dipoles and receiver detect radio emission signals as expected.

2. Measurement of the Receiver Bandwidth: After verifying that the dipole+receiver were successfully detected the radiation transmitted from the signal generator, we proceeded to measure the bandwidth of the receiver. For this, we set the amplitude of the receiver to 5 volts, and positioned the tuning-knob of the receiver to the “12 o’clock” position. Then,

starting at a transmitting frequency of 20.091 MHz we increased the transmitted frequency by steps of 1 kHz as shown in Figure 15. Our experiment shows that the bandwidth of the receiver is approximately 7 kHz. The bandpass shape of the receiver shows a double peak profile that is consequence of the electronic architecture of the receiver. Given that radio emission from Jupiter and solar flares are broader than the bandwidth of the receiver, the specific bandpass shape is not important for the detection of radio flares. This test also shows that the center frequency when the tuning-knob is at the “12 o’clock” position is approximately 20.096 MHz, however, we noticed that the central frequency can drift by several kHz.

3. Calibration of the Tuning-knob: In this experiment we set the tuning-knob to seven different positions and change the transmitted frequency of the signal generator to find the frequency of the maximum signal detected by the receiver. The results of this calibration are listed in Table 2. We found that the change in frequency when the tuning knob is turned by $\sim 45^\circ$ is approximately 50 kHz, however changes of up to ~ 90 kHz were observed when the tuning-knob was turn by that amount, which indicates non-linearity of the tuning-knob response, and fast (within few minutes) frequency drifts.

Table 2: Tuning-knob Calibration

Tuning-knob Position	Frequency (MHz)
07:30	19.897
09:00	19.989
10:30	20.037
12:00	20.089
01:30	20.139
03:00	20.206
04:30	20.243

Two other tests also showed that the receiver and dipoles were correctly working: 1. we used a commercial (**Urv: what was the name and model of the black receiver?**) 20 MHz receiver connected to our dipole array to compare the signal recorded by a commercial receiver with the signal obtained with our receiver (section 2.2). We found that the noise level recorded with both receivers was approximately the same. 2. We constantly monitor for detection of radio stations with our receiver, and in two opportunities we were able to detect radio stations, which showed that the receiver and dipoles were working as expected.

4. OBSERVATIONS

We conducted observations with the dipole radio telescope array at two different sites: the Etscorn Observatory, and the roof-top of the Workman Center building. Here we give the details of the observations conducted at both sites.

4.1. Etscorn Observations

Most of the observations reported in this work were conducted at the Etscorn Observatory. Despite of being away from the main campus buildings, the site was not ideal because of power lines located very close (within 50 m) to the dipoles, and several small buildings were also nearby. Higher radio interference events and noise levels were expected by the presence of the nearby power lines, whereas a substantial modification of the beam pattern of the combined two-dipoles was expected from the presence of nearby buildings.

The observations were conducted almost continuously from November 29, to December 27, 2005. Approximately a total of 212 Megabytes of compress data were collected during our observations with a time resolution of 0.1 s. In Figure 16 we show all the data collected during our Etscorn observations.

4.2. Workman Center Observations

The observations at the Workman Center building were conducted from March 03 to 09, and from April 04 to 18 (2006). Approximately 150 Megabytes of data were recored. In Figure 17 we show the obtained data during our Workman Center observations.

5. RESULTS AND DISCUSSION

In this section we discuss the results obtained during our Etscorn and Workman Center observations. We divided the results in two sections: description of the radio interference environment, and detection of radio signals possibly caused by the Sun. Detection of flares from Jupiter were not possible during our Etscorn observations because Jupiter enter the beam of the dipoles during day-time, when the ionosphere effectively blockages astronomical 20 MHz radiation.

5.1. Radio Interference

Perhaps the main result of our observations is the poor (radio) quality of two sites at the New Mexico Tech campus where our observations were conducted. The presence of power lines close to the Etscorn observatory and internal power lines, computers, and metallic structure of the Workman Center building generated substantial radio interference that could mask detection of solar and Jovian flares.

The RFI detected during our observations may be classified in three main groups: short-RFI (few seconds), long-RFI (several minutes), and very long-RFI (several hours). In figures 18 to 20 we show examples of these three types of RFI. Here we give a brief description of them:

Short-RFI Events (Figure 18): RFI spikes that lasted for less than a few seconds were frequently detected principally during day time, from approximately 07 to 20 hours MST. We found that even turning on and off the light in the receiver room would produce this kind of interference.

Long-RFI Events (Figure 19): RFI signals that lasted for several minutes, and that could have been caused by the superposition of many short-RFI events that lasted for several minutes. We find likely that RFI generated close to the dipole site could be one of the main causes for this type of RFI (e.g., due to the opening and closing of the domes at the Etscorn Observatory). This type of RFI could be easily mistaken as a Jovian radio burst (e.g., see Kraus 1986).

Very Long-RFI Events (Figure 20): We define Very long-RFI signals as events that systematically raised the bandpass level during several hours. Several of such an events were detected during our observations.

5.2. Possible Detection of the Sun

One of the characteristics of the data that can be easily observed directly from Figures 16 and 17 is that the RFI occurs mainly during day-time hours. Obviously, this is in part caused by local RFI sources that are more active during the day, but also could be consequence in part from changes in the reflectivity of the ionosphere. Changes in the ionosphere are caused by radiation from the Sun, thus the detection of a greater number of RFI events due to a change in the properties of the ionosphere is an indirect detection of the Sun's radiation. In addition, we detected a few events that may be caused by indirect and/or direct detection of solar radiation.

One of such an events is shown in Figure 21. First note the occurrence of RFI spikes between 06 and 15 hours that, as discussed above, could be caused by local and distant sources of RFI given changes in the reflectivity of the ionosphere by the Sun’s radiation. But in addition, note how the baseline level is higher between 11 and 18 hours MST. This higher baseline level approximately coincides with the time of the day when the Sun was mostly within the beam of the dipoles. Thus, the high baseline level could be caused a combination of direct detection of 20.1 MHz radiation from the Sun, and a more active ionosphere at 20.1 MHz modulated by Sun radiation. This high bandpass level is not caused by the additive effect of more frequent RFI spikes because the density of RFI events between 06 and 10 hours MST is not so different than the density of RFI events between 11 and 15 hours MST, and in the 06 to 10 hours MST period we detected no rise in the baseline level (see Figure 21). We note that we did not always detect such an increase in the baseline level when the Sun was within the beam of the dipoles. This implies that the rise in the baseline level shown in Figure 21 cannot only be caused by detection of 20 MHz radiation from the Sun, but must have contribution from another source of radiation. Finally, we cannot rule out that such an increase in the baseline level is caused by a weak very long-RFI event.

Another type of event that could indicate indirect detection of the solar influence on the ionosphere is exemplified in Figure 22. The increase of the baseline level during sunrise suggests that solar radiation might have modified the physical properties of the ionosphere. As in the type of events exemplified in Figure 21, we did not always detect a clear rise in the baseline level during sunrise, nor we can rule out very long-RFI signals that could be causing the rise in the baseline.

We compared our data with the solar and Jovian radio data from <http://jovearchive.gsfc.nasa.gov/cgi-bin/calendar/calendar.cgi> to look for detection of Jovian and solar radio burst. We found no clear detection of a flare in our data with respect to that data base.

6. POTENTIAL USE OF THE DIPOLE ARRAY FOR A STUDENT LABORATORY

The Dipole Radio Telescope developed in this project is perfectly suitable to be used as an educational instrument to introduce undergraduate students to the field of long wavelength radioastronomy. A laboratory using this simple radio telescope will allow the students to:

1. Learn about the origins of long wavelength radioastronomy, and about the astrophysical processes that can produce detectable radio emission at 20 MHz.

2. Work with a simple two element dipole array. This array is suitable to be used as an introductory instrument to study the basics of interferometry and beam steering.
3. Recognize the importance of the ionosphere in long wavelength observations.
4. Realize the problematic of radio frequency interference in the field of radio astronomy, particularly at long wavelengths.
5. Conduct real radioastronomical observations, analyze data, and reach conclusions based on the observations.

A downside of the use of the Dipole Radio Telescope reported in this work by undergraduate students is the impossibility to predict with 100% certainty the occurrence of a burst during the observations. In addition, to increase the chances of success, it would be better to conduct the observations far from buildings and power lines, and during night time for detection of Jovian flares. These requirements clearly introduce logistics problems. Nevertheless, even observing in poor RFI environments (such as Workman Center or the Etscorn Observatory) the students will be able to accomplish the goals stated above.

Here we suggest the procedure to be followed by undergraduate students to conduct observations with the Dipole Array constructed in this project.

PRELIMINARY WORK

- 1. History of Long Wave Radio Astronomy:** As a first approach to the field of long wave radio astronomy, the students may write a small summary about the history of this field, particularly the early history of solar and Jovian observations. Excellent and highly enjoyable references that the students may consult are the papers by Kundu, Franklin, and Drake in *Serendipitous Discoveries in Radio Astronomy* (1983).
- 2. Radio Emission from Astronomical Sources:** The students should study and summarize the general characteristics of radio emission from astronomical objects. In particular, Galactic radio noise, and radio emission from the Sun and Jupiter. A classic reference that the students may use is Chapter 8 in Kraus (1986).
- 3. The Dipole Radio Telescope:** The students should be required to prepare a summary of the characteristics of the Dipole Radio Telescope. The recommended references are the Radio-JOVE manual and/or this document.

PLANNING THE OBSERVATIONS

- 1. When to observe:** The observations should be carefully scheduled to increase the chances of detection of an astronomical radio signal. In the case that the goal is to detect

Jovian radio flares, then the observations should be conducted when the transit of Jupiter occurs during the night. The use of an astronomical ephemeris computer program such as Xephem (in Linux) is recommended to obtain the transit time of Jupiter. The students may also check the site <http://radiojove.gsfc.nasa.gov/control/predictions.htm> where predictions of Jovian flares are tabulated. To highly increase the chances of detecting Jovian emission, the students should observe when predicted Jovian activity approximately coincides with the transit of Jupiter.

2. Where to observe: As mentioned before, RFI at the Etscorn Observatory and at the Workman Center building highly compromise the chances of detecting radio flares from Jupiter. Thus, to increase the probability of success, the observations should be conducted at a site far (several hundred meters away) from power lines and buildings. Nevertheless, observations may be attempted at the Workman Center that is a quite convenient location to setup the receiver and computer.

OBSERVATIONS AND DATA REDUCTION

1. Observations: In this section the students are expected to describe the details of the observations. When and where were the observations conducted?, What was the operating system used to record the data?. The students should also describe the site where the observations were conducted, in particular the location of power lines and other sources of RFI.

2. Data Reduction, Analysis and Conclusions: The data may be plotted as a function of local, LSR, or UT time. In the case that the data was recorded using SkyPipe in Windows, then the data may be exported to ASCII using the Python program listed in Appendix B. Then the students should explore the data to look for burst candidates. The candidates can be confirmed by comparing with data reported in sites of low frequency radio observations such as <http://jovearchive.gsfc.nasa.gov/cgi-bin/calendar/calendar.cgi> and <http://www.ips.gov.au/Solar/2/6>. Finally, general and specific conclusions should be reported based on the results and data analysis.

7. SUMMARY

We report the details of the construction of two two-element dipole array antennas, and the construction of two 20.1 MHz heterodyne receivers. This equipment is intended for the detection of decameter radiation from solar and Jovian bursts. We performed several tests of the equipment and empirically characterized its frequency range, bandwidth, and bandpass shape.

We conducted observations at two different sites in the New Mexico Tech campus: first at the Etscorn Observatory, and then on the roof-top of the Workman Center building. In total, we collected approximately 48 full days of data at a sample rate of 0.1 s that resulted in approximately 360 Megabytes. Our observations show intense radio interference at both sites, mainly during the day time, that could easily mask astronomical radio burst. We classify the RFI in three groups depending on its duration. The type classified as long-RFI events could be easily confused with Jovian flares (e.g., Kraus 1986). We compare our observations with the data set in <http://jovearchive.gsfc.nasa.gov/cgi-bin/calendar/calendar.cgi> to search for flares and found no clear detection. Nevertheless, we detected changes in the baseline levels that could be caused by indirect detection of solar radiation.

We developed a Python program to convert data from the SkyPipe Windows format (SPD) to ASCII to be able to more conveniently analyze the data. In addition, a Python program was created to record the signal from two different receivers simultaneously using a computer running on Linux. The Linux software developed in this project also calculates and displays the dynamic spectrum of the signal.

We also reviewed the details of dipole antenna and two-dipole arrays radiation patterns in free space and near the ground (see Appendix A), and model different radiation patterns when physical parameters of the dipole configuration are changed. The modeling was done in Python using a program developed by one of us¹¹.

The dipole array telescope developed in this work is perfectly suitable for an undergraduate laboratory. We present the goals that could be accomplished by the use of this instrument in an undergraduate laboratory project. We also present recommendations for the preliminary work, the planning of the observations, and the different parts that an undergraduate report based on observations with this instrument may have.

We acknowledge Dr. Dave Westpfahl for providing the funds to purchase two Radio Jove antenna and receiver kits, and for the use of laboratory equipment for the construction of the antennas and receivers.

A. Dipole antenna (array) radiation patterns

Single center-fed dipole in free space

¹¹All Python routines were developed by U. R. V.

The radiation pattern of a current element in free space can be computed as follows.

The vector potential is computed from the current distribution in the dipole wire.

$$\bar{A}(\bar{x}) = \frac{\mu_0}{4\pi} \frac{e^{ikr}}{r} \int \bar{J}(\bar{x}') d^3x' \quad (\text{A1})$$

The far field \bar{E} and \bar{B} fields are computed as follows.

$$\bar{H} = \frac{ik}{\mu_0} \hat{n} \times \bar{A} \quad (\text{A2})$$

$$\bar{E} = Z_0 \bar{H} \times \hat{n} \quad (\text{A3})$$

The radiation power pattern is then given as follows.

$$\frac{dP}{d\Omega} = \frac{1}{2} \text{Re} [r^2 \hat{n} \cdot \bar{E} \times \bar{H}] = \frac{Z_0}{2} \text{Re} [r^2 \bar{H} \times \hat{n} \times \bar{H}^*] = \frac{Z_0 r^2}{2} |\bar{H}|^2 \quad (\text{A4})$$

Consider a center-fed dipole of total length d , aligned along the z axis, (with $k = 2\pi/\lambda$),

$$\bar{J}(\bar{x}) = I \sin\left(\frac{kd}{2} - k|z|\right) \delta(x)\delta(y) \hat{z} \quad (\text{A5})$$

This gives

$$\bar{A}(\bar{x}) = \frac{\mu_0}{4\pi} \frac{2I e^{ikr}}{kr} \left[\frac{\cos\left(\frac{kd}{2} \cos\theta\right) - \cos\left(\frac{kd}{2}\right)}{\sin^2\theta} \right] \hat{z} \quad (\text{A6})$$

Therefore with $\hat{n} = \hat{r}$ and with $kd = \pi$ for a half-wave dipole,

$$\bar{H} = \frac{-Ii}{2\pi} \frac{e^{ikr}}{r} \left[\frac{\cos\left(\frac{\pi}{2} \cos\theta\right)}{\sin\theta} \right] \hat{\phi} \quad (\text{A7})$$

$$\bar{E} = \frac{+Z_0 Ii}{2\pi} \frac{e^{ikr}}{r} \left[\frac{\cos\left(\frac{\pi}{2} \cos\theta\right)}{\sin\theta} \right] \hat{\theta} \quad (\text{A8})$$

$$\frac{dP}{d\Omega} = \frac{Z_0 r^2}{2} |\bar{H}|^2 = \frac{Z_0 I^2}{8\pi^2} \left[\frac{\cos^2\left(\frac{\pi}{2} \cos\theta\right)}{\sin^2\theta} \right] \quad (\text{A9})$$

This power pattern is shown in Figure 2.

Single horizontal dipole near the ground

The ground can be approximated as an infinitely large flat conductor with the dipole placed at a height h above it, still aligned parallel to the z axis.

For a perfect electric conductor, incident waves are completely reflected. At any observation point given by \hat{n} , there are contributions from the real dipole, as well as reflections which can be modeled using a virtual dipole (image) below the surface of the conductor. The E and B fields above the ground are result of the coherent superposition of the fields from the real and virtual dipoles. The fields below the ground (inside the conductor) are zero.

At the surface of the conductor, the tangential components of E must vanish. For a horizontal dipole, by the geometry of reflection of normal E components, the virtual dipole has its current in the opposite direction as the real dipole, and contributes E and B fields out of phase by π radians from those of the real dipole (a sign change).

In the far field,

$$r_r = r - h \cos\psi \quad (\text{A10})$$

$$r_v = r + h \cos\psi \quad (\text{A11})$$

where ψ is the angle between \hat{r} and the y axis such that $\cos\psi = \sin\theta\sin\phi$. Also, make the further approximation that for amplitude variations, $r_r = r_v = r$ Therefore,

$$\bar{H} = \frac{-Ii}{2\pi} \left[\frac{\cos\left(\frac{\pi}{2}\cos\theta\right)}{\sin\theta} \right] \left(\frac{e^{ikr_r}}{r_r} - \frac{e^{ikr_v}}{r_v} \right) \hat{\phi} \quad (\text{A12})$$

where

$$\left(\frac{e^{ikr_r}}{r_r} - \frac{e^{ikr_v}}{r_v} \right) = \frac{e^{ikr}}{r} (e^{-ikh\cos\psi} - e^{+ikh\cos\psi}) = \frac{-2ie^{ikr}}{r} \sin(kh\cos\psi) \quad (\text{A13})$$

Therefore,

$$\frac{dP}{d\Omega} = \frac{Z_0 I^2}{2\pi^2} \left[\frac{\cos^2\left(\frac{\pi}{2}\cos\theta\right)}{\sin^2\theta} \right] \sin^2\left(\frac{\pi h}{d} \sin\theta \cos\phi\right) \quad (\text{A14})$$

The power pattern is shown in Figures 3 and 4 for various heights above the ground. The multiplicative interference pattern depending on the distance between the dipole and its virtual image, modifies the radiation pattern of a dipole in free space. A height can be chosen so as to aim the direction of maximum intensity at a particular position in the sky.

Two element dipole array near the ground

Consider two dipoles placed a distance b apart from each other, both at a height h from the ground (infinite flat conductor), and still aligned parallel to the z axis with the baseline along the x axis.

Here, a coherent superposition of the contributions from the two dipoles and their images gives

$$\bar{H} = \frac{-Ii}{2\pi} \left[\frac{\cos\left(\frac{\pi}{2}\cos\theta\right)}{\sin\theta} \right] \left(\frac{e^{ikr_{1r}}}{r_{1r}} - \frac{e^{ikr_{1v}}}{r_{1v}} + \frac{e^{ikr_{2r}}}{r_{2r}} - \frac{e^{ikr_{2v}}}{r_{2v}} \right) \hat{\phi} \quad (\text{A15})$$

Here,

$$r_{1r} = r - h \cos\psi \quad (\text{A16})$$

$$r_{1v} = r + h \cos\psi \quad (\text{A17})$$

$$r_{2r} = r - h \cos\psi - b \cos\eta + \alpha \quad (\text{A18})$$

$$r_{2v} = r + h \cos\psi - b \cos\eta + \alpha \quad (\text{A19})$$

where η is the angle between \hat{r} and the x axis such that $\cos\eta = \sin\theta\cos\phi$. α is an arbitrary phase difference between the signals of the two independent dipoles. It corresponds to the phase delay brought about by a phasing cable used to steer the beam.

The term in parentheses in \bar{H} becomes

$$= \frac{e^{ikr}}{r} \left(e^{-ikh\cos\psi} - e^{ikh\cos\psi} + e^{ik(-h\cos\psi - b\cos\eta + \alpha)} - e^{ik(h\cos\psi - b\cos\eta + \alpha)} \right) \quad (\text{A20})$$

$$= \frac{-2ie^{ikr}}{r} \sin(kh\cos\psi) \ 2\cos\left(\frac{kb}{2}\cos\eta + \frac{\alpha}{2}\right) e^{ikb\cos\eta} \quad (\text{A21})$$

Therefore,

$$\frac{dP}{d\Omega} = \frac{2Z_0I^2}{\pi^2} \left[\frac{\cos^2\left(\frac{\pi}{2}\cos\theta\right)}{\sin^2\theta} \right] \sin^2\left(\frac{\pi h}{d}\sin\theta\cos\phi\right) \cos^2\left(\frac{\alpha}{2} + \frac{\pi b}{2d}\sin\theta\cos\phi\right) \quad (\text{A22})$$

The combined power pattern is a product of the radiation pattern of a single dipole, one interference term due to an out of phase virtual source, and a second interference term due to the phase difference between the two dipoles. The radiation pattern can change by varying the height of the dipoles, the spacing between them, or the length of a phasing cable. See figures 5, 6, and 7.

B. Python Program to Convert Data from SPD to ASCII Format

```
def spd2txt(filename, txtfilename, mode='a'):  
    """ Convert an spd file to a column based text file.  
    filename [] : input spd file  
    txtfilename [] : output text file  
    mode ['a'] : file access mode ('w','a').  
    """  
    time,data = readspd(filename);  
    writetofile(txtfilename,mode,time,data);
```

```
def readspd(filename='test.spd'):  
    fp = open(filename,'r');  
  
    junk = fp.read(10);  
    start = arr2double(fp.read(8));  
    finish = arr2double(fp.read(8));  
    lat = arr2double(fp.read(8));  
    lng = arr2double(fp.read(8));  
    maxy = arr2double(fp.read(8));  
    miny = arr2double(fp.read(8));  
    timezone = arr2int(fp.read(2));  
    source = fp.read(10);  
    author = fp.read(20);  
    localname = fp.read(20);  
    location = fp.read(40);  
    channels = arr2int(fp.read(2));  
    notelength = arr2int(fp.read(4));  
    note = fp.read(notelength[0]);  
  
    print 'Header : '  
    print 'start : ', start[0]  
    print 'finish : ',finish[0]  
    print 'lat,lng : ', lat[0], lng[0]  
    print 'maxy,miny : ',maxy[0],miny[0]  
    print 'timezone : ', timezone[0]  
    print 'source : ',source  
    print 'author : ',author  
    print 'localname : ',localname  
    print 'location : ',location
```

```
print 'channels : ',channels[0]
print 'notelength : ',notelength[0]
print 'note : ',note

timebytes = 8;
databytes = 8;
if(string.find(note,'Integer Save') >=0):databytes=2;

floc = fp.tell();
print "Location in file : ", floc
sizoff = filesizebytes(filename);
print "Size of file : ",sizoff;
lentoread = sizoff - floc;
print "reading ", lentoread," bytes."
N=lentoread/16;
print "reading ", N ," data points."

rang = range(0,N);
time = array.array('d',rang);
data = array.array('d',rang);
for i in rang:
    time[i] = (arr2double(fp.read(8)))[0];
    data[i] = (arr2double(fp.read(8)))[0];

fp.close();
return time,data;

def arr2double(arr):
    tmp = array.array('d',arr);
    return tmp;

def arr2int(arr):
    tmp = array.array('h',arr);
    return tmp;

def filesizebytes(fname):
    pip = os.popen('wc -c ' + fname);
    outp = pip.read();
    pip.close();
    sizoff = int((outp.split())[0],10);
```

```
    return sizoff;

def filesize(fname):
    pip = os.popen('wc -l ' + fname);
    outp = pip.read();
    pip.close();
    sizoff = int((outp.split())[0],10);
    return sizoff;

def writetofile(fname,mode,time,data):
    num = len(time);
    print 'Writing ',num,'lines to ', fname
    fp = open(fname,mode);
    for i in range(0,num):
        fp.write(str(time[i]) + " " + str(data[i]) + str('\n'));
    fp.close();

def getlistoffiles(rootpath):
    """ Get a list of files under "rootpath"
    rootpath [] : path for a day of data
    """
    pip = os.popen('ls ' + rootpath + '/*');
    flist = pip.read();
    pip.close();
    return flist.split();

def convertall(rootpath,txtfilename):
    """ Convert all spd files in this directory into
    text format, and concatenate into a single txt file
    rootpath [] : directory of spd files
    txtfilename [] : output text file name
    """
    flist = getlistoffiles(rootpath);
    for ff in flist:
        spd2txt(ff,txtfilename);
    plotpower(txtfilename);
```

C. Data Recording/Handling Software for Linux.

```
import ossaudiodev as osd
import string
import array
import Numeric as num
import FFT
import os
import pipes
import pylab as pl
import time as timer
import signal

#
# Child : Send timestamp and N points over the pipe - every 0.1 second
# Parent : Loop for each 0.1 second [sec]
#           Read timestamp and N points : time[0.1 sec]
#           Calc spectrum on N points : spectrum[sec]
#

# Record for NSEC seconds.
def start(NSEC=4,disp=0,outfile="DAT/jove",tpf=4):
    (fr,fw)=os.pipe();
    childpid = os.fork();

    SRATE = 8000;
    N = SRATE/10; # must be a multiple of P
    NDAT = NSEC*10;

    if(childpid==0):
        # Child : Read in from the sound card
        print "Child Process"
        qq = osd.open('/dev/audio','r');
        qq.setfmt(osd.AFMT_U16_LE)
        qq.channels(1)
        qq.speed(SRATE)

        print 'Recording for ',NSEC, ' seconds';
```

```
print "Recording ", NDAT, " samples"

print "Start Recording..."
for tt in range(0,NDAT):
    os.write(fr,qq.read(N*2));
print "End Recording."

else:
    # Parent : Compute power, spectrum and write to disk
    print "Parent Process"
    P=4;
    gdata = array.array('H');
    spect = array.array('d',range(0,N/P));

    if(dispatch):
        ND = 100;
        power = pl.array(range(0,ND),'d');
        time = pl.array(range(0,ND),'d');
        power[0]=3e+8;
        for i in range(1,ND):
            power[i]=0.0;
            time[i]=time[i]/10;
        pl.ion();
        line, = pl.plot(time,power,'k');
        pl.xlabel('Time (0.1 sec)');
        pl.ylabel('Power');
        pl.draw();

        for tt in range(0,NDAT):
            if(tt%(tpf*10)==0):
                powerfile, specfile = createfilenames(outfile);
                fp = open(powerfile,'w');
                fs = open(specfile,'wb');
                nums = array.array('d',[N/P]);
                nums.tofile(fs);
                print "Recording " + powerfile + ".spec";

        gdata = array.array('H',os.read(fr,N*2));
        glen = len(gdata);
```

```
spec = abs(FFT.real_fft(gdata,n=glen));
powerval = sum(spec);
timeval = timer.time();

if(dispatch):
    power[ND-1] = powerval;
    line.set_data(time,power);
    pl.draw();
    for i in range(0,ND-1):
        power[i]=power[i+1];

# Average P channels.
#print glen, len(spec), N/P
k=0;
for j in range(0,len(spec-1),P):
    spect[k]=sum(spec[j+1:j+1+P]);
    k=k+1;
#for j in range(0,N/P):
# spect[j]=spec[j+1];
spect.tofile(fs);
wstr = str(timeval)+str(" ") +str(powerval)+str('\n');
fp.write(wstr);

if((tt+1)%(tpf*10)==0 or tt+1==NDAT):
    fp.flush();
    fp.close();
    fs.flush();
    fs.close();
    print "Done : " + timer.asctime()

print "Closing child process"
os.kill(childpid,signal.SIGKILL);
if(dispatch):
    pl.clf();
    pl.ioff();

# Create meaningful file names
def createfilenames(outfile):
    tim = (timer.asctime()).split();
```

```
tstr = tim[3];
tims = "_" + tim[4] + "_" + tim[1] + "_" + tim[2] + "_" + tstr[0:2] + "_" + tstr[3:5] + "_" + tstr[6:8];
powerfile = outfile + tims + ".power";
specfile = outfile + tims + ".spec";
return powerfile, specfile

# Make power and spectrum plots
def makeplots(fileroot,t1=0,nt=-1):
    datafile = fileroot + ".power";
    specfile = fileroot + ".spec";
    #pl.ion();
    pl.subplot(211);
    plotpower(datafile,t1,nt);
    pl.subplot(212);
    plotspectrum(specfile,t1,nt);
    #pl.ion();
    pl.show();

# Plot power vs time
def plotpower(filename,t1,nt):
    time,power = readdatafile(filename);
    if(nt<0 or nt>(len(time)-t1)):
        nt = len(time)-t1;
    timm = range(0,len(time));
    pl.cla();
    pl.title(filename);
    pl.xlabel('Time');
    pl.ylabel('Power');
    pl.plot(timm[t1:t1+nt],power[t1:t1+nt], 'k')

# Plot dynamic spectrum
def plotspectrum(filename,t1,nt):
    freq,spectrum = readspecfile(filename);
    if(nt<0 or nt>(len(spectrum[0])-t1)):
        nt = len(spectrum[0])-t1;
    pl.cla();
    #pl.title(filename);
    pl.xlabel('Time (0.1 sec)');
    pl.ylabel('Frequency');
    #pl.pcolor((spectrum),shading='flat');
```

```
pl.pcolor((spectrum[0:(len(spectrum)/2),t1:t1+nt]),shading='flat',cmap=pl.matplotlib.cm.hot);
#pl.pcolor((spectrum[0:len(spectrum),t1:t1+nt]),shading='flat');
#pl.pcolor((spectrum),shading='flat',cmap=pl.matplotlib.cm.hot);

# Read the power data file
# Take in number of lines as an input param
def readdatafile(fname):
    flen = filesizelines(fname);
    rang = range(0,flen);
    time = array.array('d',rang);
    data = array.array('d',rang);

    fp = open(fname,'r');
    for i in range(0,flen):
        lstr = fp.readline();
        splitstr = lstr.split();
        time[i] = float(splitstr[0]);
        data[i] = float(splitstr[1]);
    fp.close();
    return time,data;

# Read spectrum data file
# Take in number of lines as an input param
def readspectfile(fname):
    nbytes = filesizebytes(fname);
    ff = open(fname,'rb');
    nums = array.array('d');
    nums.fromfile(ff,1);
    NP = int(nums[0]);
    NDAT = (nbytes-1)/(NP*8);
    spectrum = pl.zeros((NP),NDAT,'d');
    freq = pl.array(range(0,NP)*10,'d');
    for tt in range(0,NDAT):
        aspec = array.array('d');
        aspec.fromfile(ff,NP);
        spectrum[0:(NP),tt] = aspec;
    ff.close();
    return freq,spectrum;
```

REFERENCES

Please check your references, the city of publication and edition are missing in some of them. I am using the reference format of the ApJ.

Balanis A.C. 1996, in Antenna Theory, analysis and design

Bagenal, F. et al., 2004, Jupiter - The planet, satellites and magnetosphere, (Cambridge Univ. Press)

Drake, F. D. 1983, in Serendipitous Discoveries in Radio Astronomy, ed., K. Kellermann, & B. Sheets (Green Bank: NRAO), 258

Franklin, K. L. 1983, in Serendipitous Discoveries in Radio Astronomy, ed., K. Kellermann, & B. Sheets (Green Bank: NRAO), 252

Jackson J.D. 2004, Classical Electrodynamics (Third ed.; New York: John Wiley & Sons, Inc.)

Kraus, J. D. 1986, Radio Astronomy (Second ed.; Ohio: Cygnus-Quasar Books)

Kundu, M. R. 1983, in Serendipitous Discoveries in Radio Astronomy, ed., K. Kellermann, & B. Sheets (Green Bank: NRAO), 247

Kundu, M. R. 1965, Solar Radio Astronomy (John Wiler and Sons.)

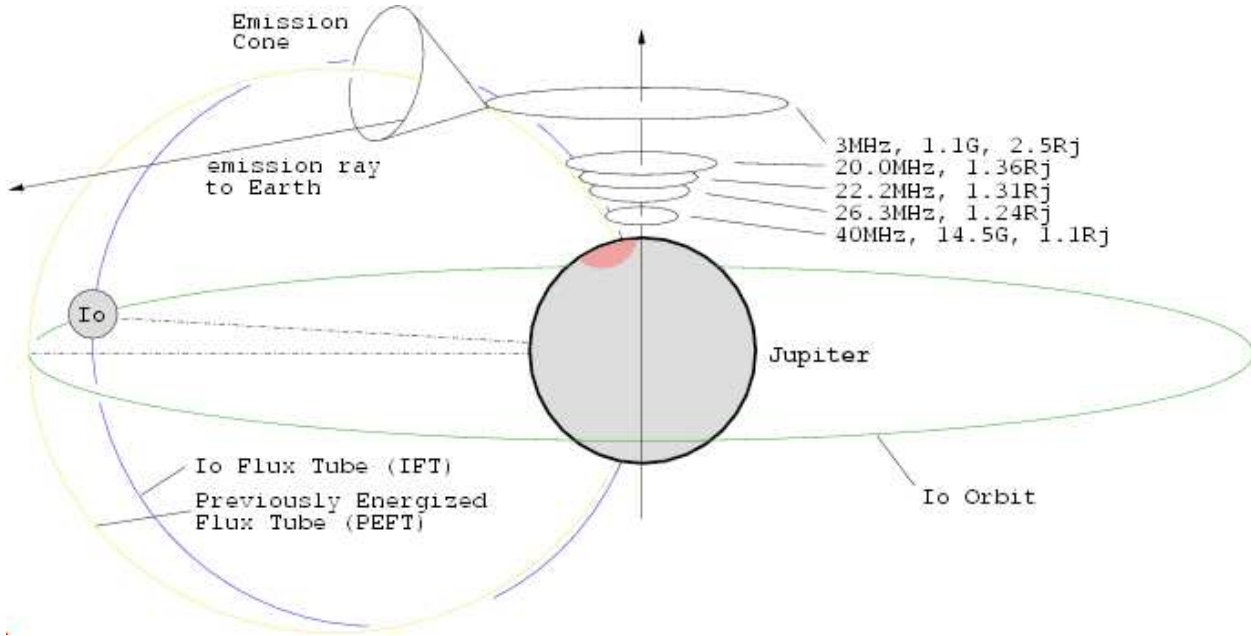


Fig. 1.— Schematic explaining the origin and mechanism of Jupiter's Decametric Emission (<http://www.jupiter.radio.com/jove-emission.php>).

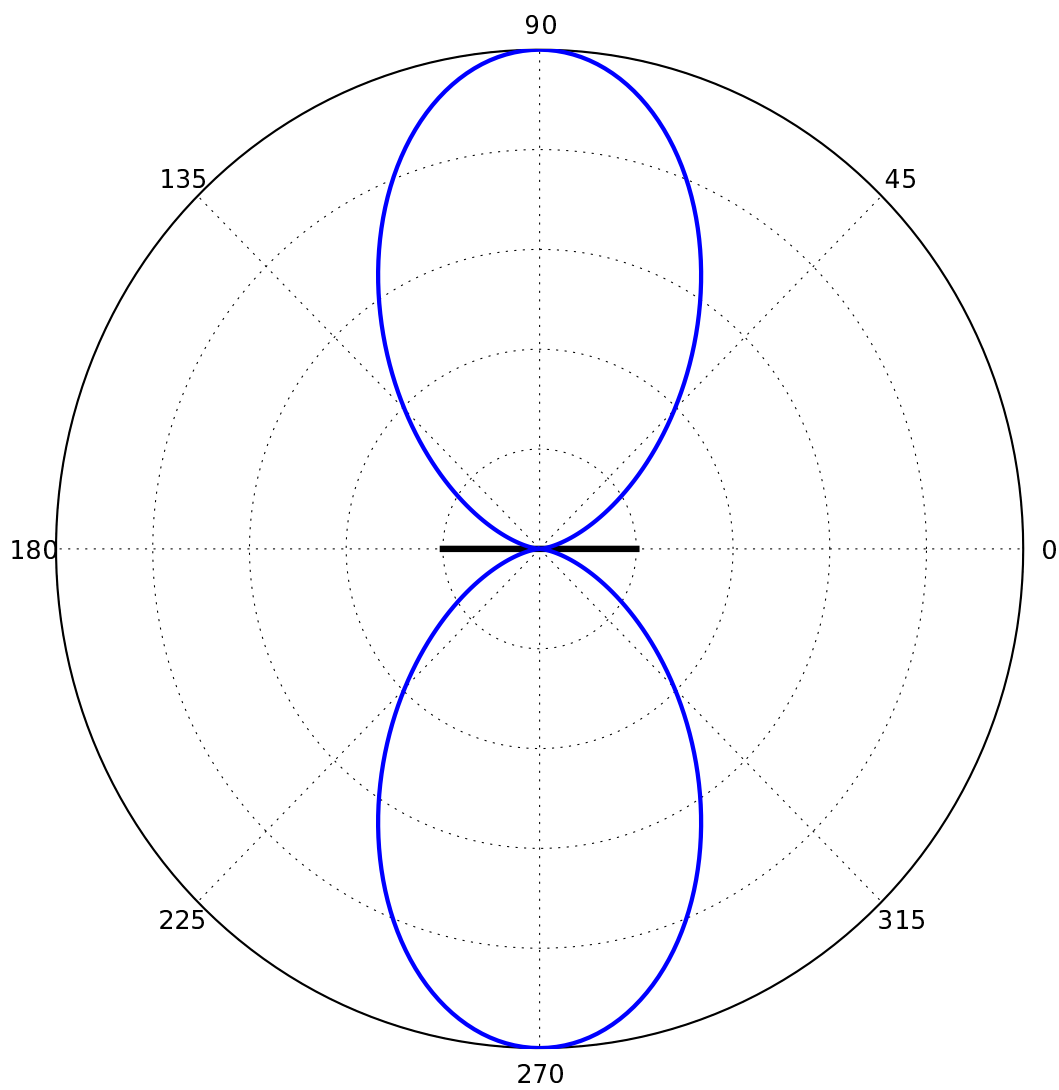


Fig. 2.— Antenna radiation pattern of a single dipole in free space.

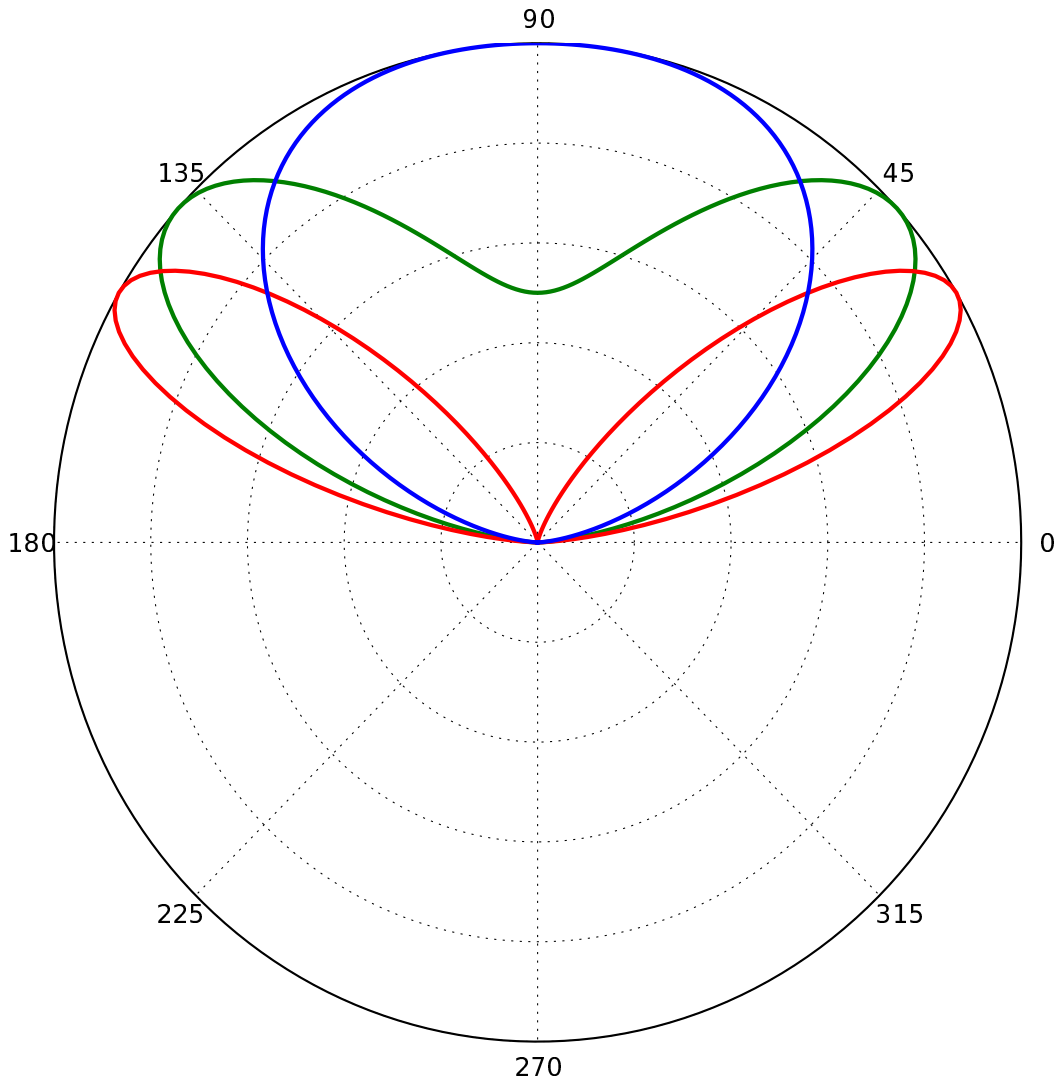


Fig. 3.— Beam pattern of a single dipole above the ground at three different heights: $h/d = 0.5$ (*blue*), 0.75 (*green*), 1.0 (*red*), where h/d is the height of the dipole divided by its length. As the height above the ground is increased, the shape changes and the number of lobes increases.

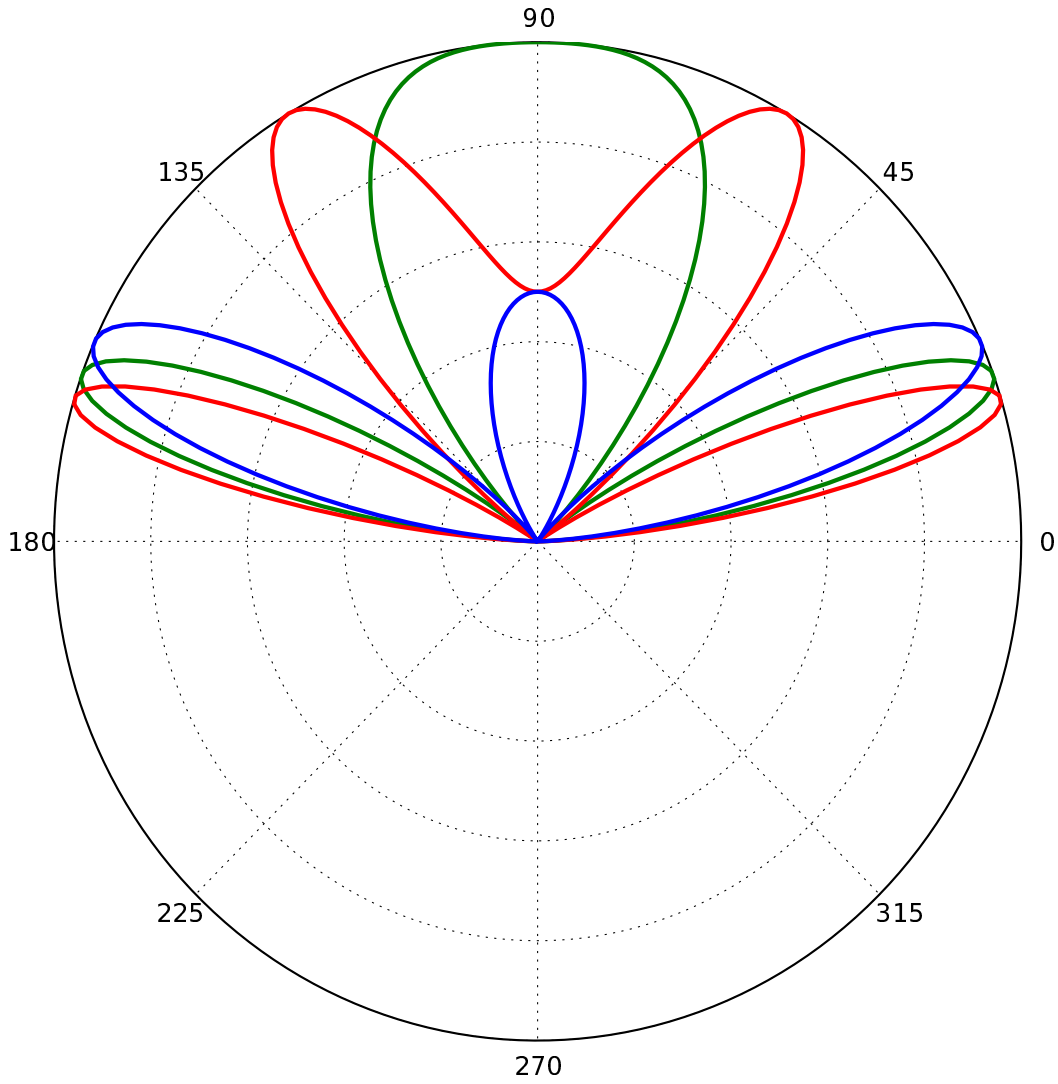


Fig. 4.— Beam pattern of a single dipole above the ground at three different heights: $h/d = 1.25$ (*blue*), 1.50 (*green*), 1.75 (*red*). Compare with Figures 2,3. At heights equal to or greater than $\lambda/2$, there are more than two interference lobes.

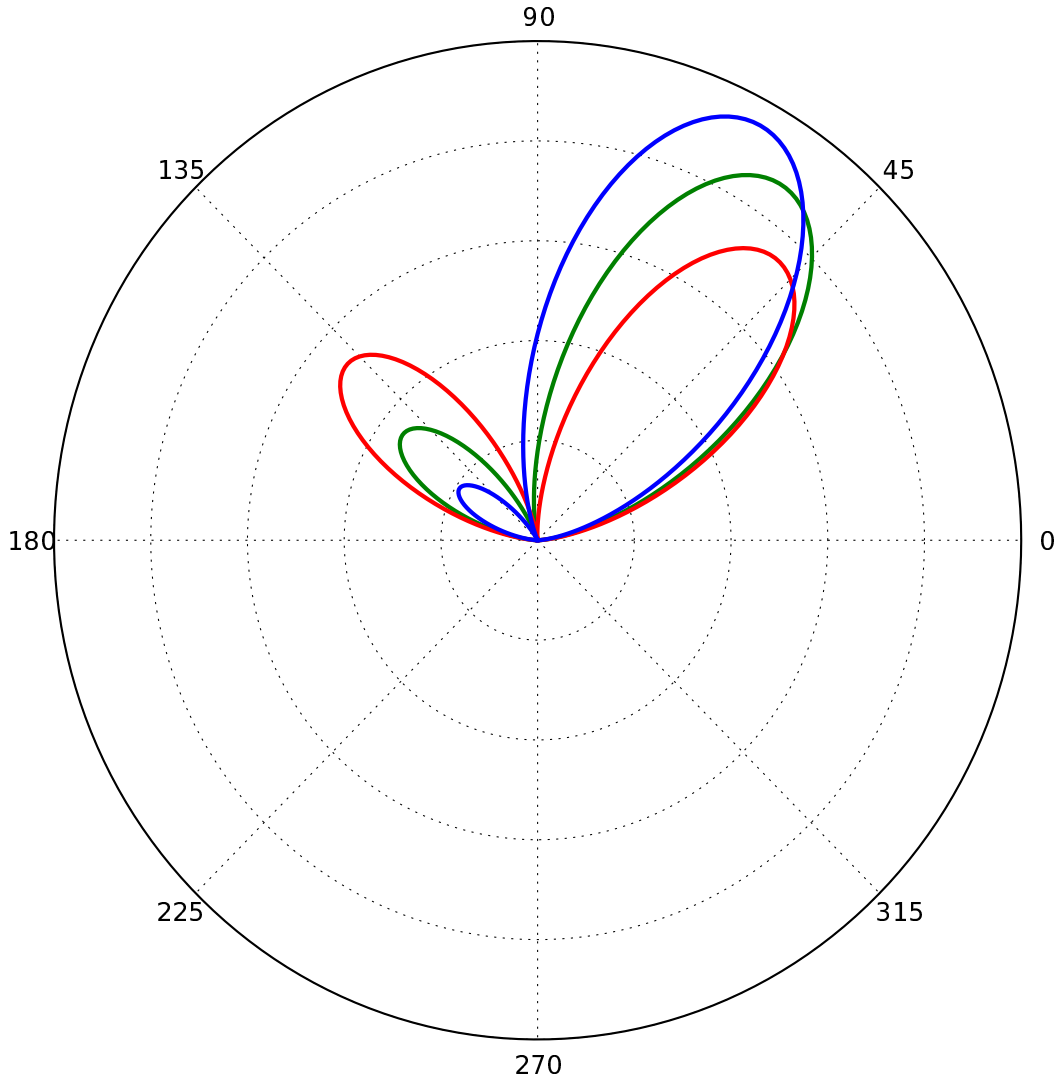


Fig. 5.— Beam pattern of a two-dipole array with delay phases of $\alpha = -100^\circ$ (*blue*), -130° (*green*), -160° (*red*). This phase delay can be supplied via a phasing cable of certain length, and can be used to steer the beam of the antenna. Steering to lower elevations (decreases the gain in the preferred direction, and increases the size of the back-lobe).

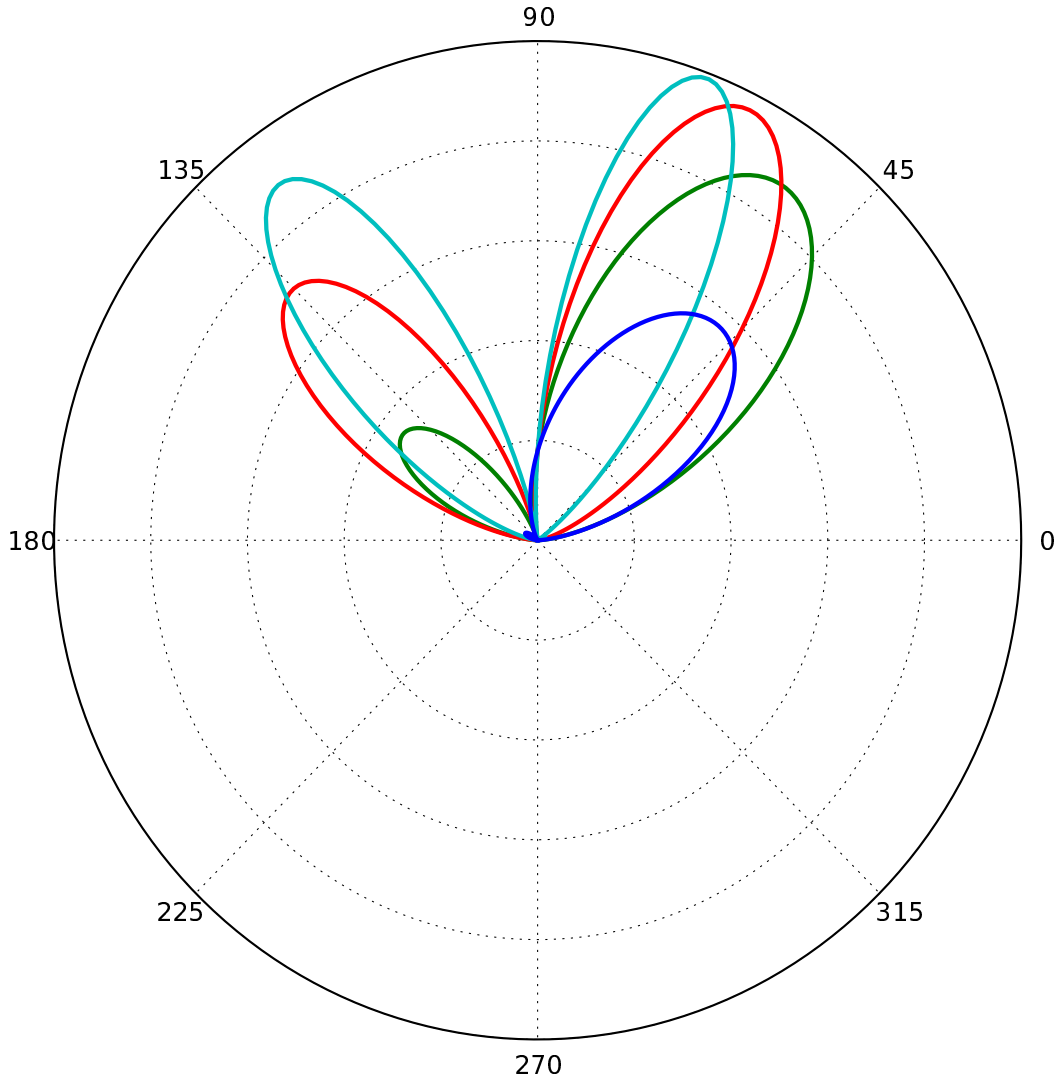


Fig. 6.— Beam pattern of a two-dipole array with varying baseline length. $b/d = 0.5$ (*blue*), 1.0 (*green*), 1.5 (*red*), 2.0 (*sky-blue*). b is the length of the baseline, and d is the length of the dipole. Increasing the baseline length (b) increases the resolution of the beam (narrower beam), and gives a higher gain. However, back-lobes also appear and increase in size.

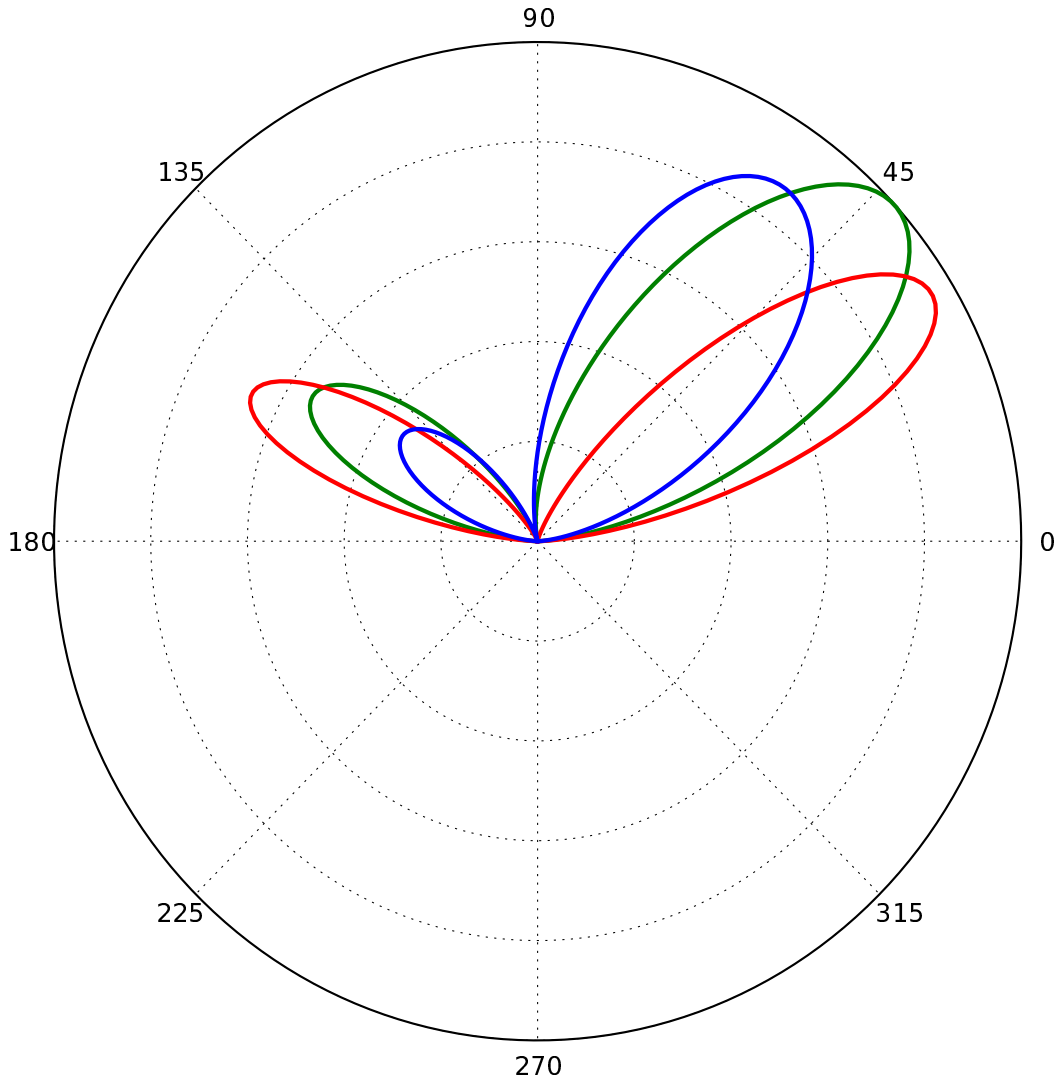


Fig. 7.— Beam pattern of a two-dipole array with varying height. $h/d = 0.5$ (*blue*), 0.75 (*green*), 1.0 (*red*). Once a suitable baseline and phasing length is chosen, changing the height of the dipoles can effectively steer the beam in elevation. Here too, at greater heights as the beam is steered towards lower elevations, the size of the back lobe increases.

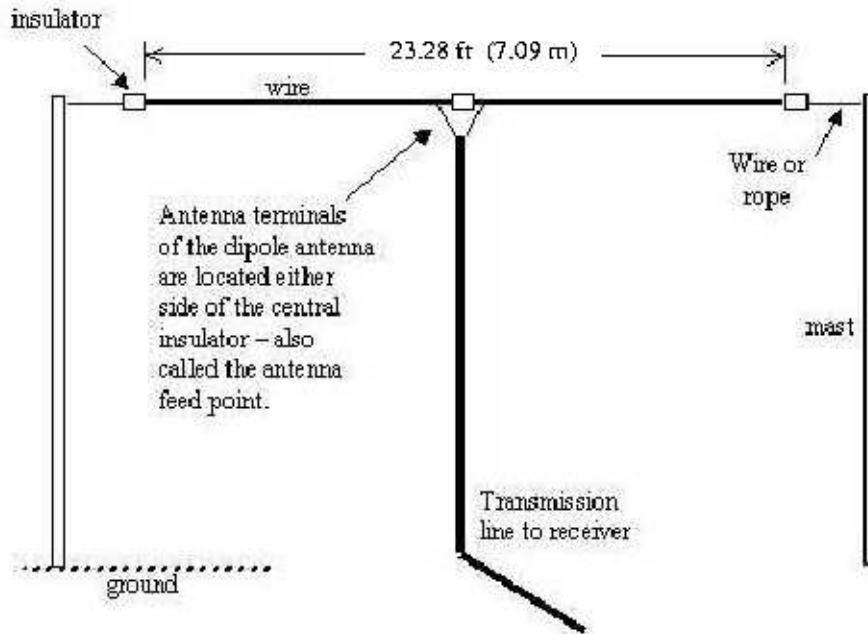


Fig. 8.— Scheme of one dipole antennas built in this project (figure from the Jove RJ1.2 Antenna Manual, Dec 2004).

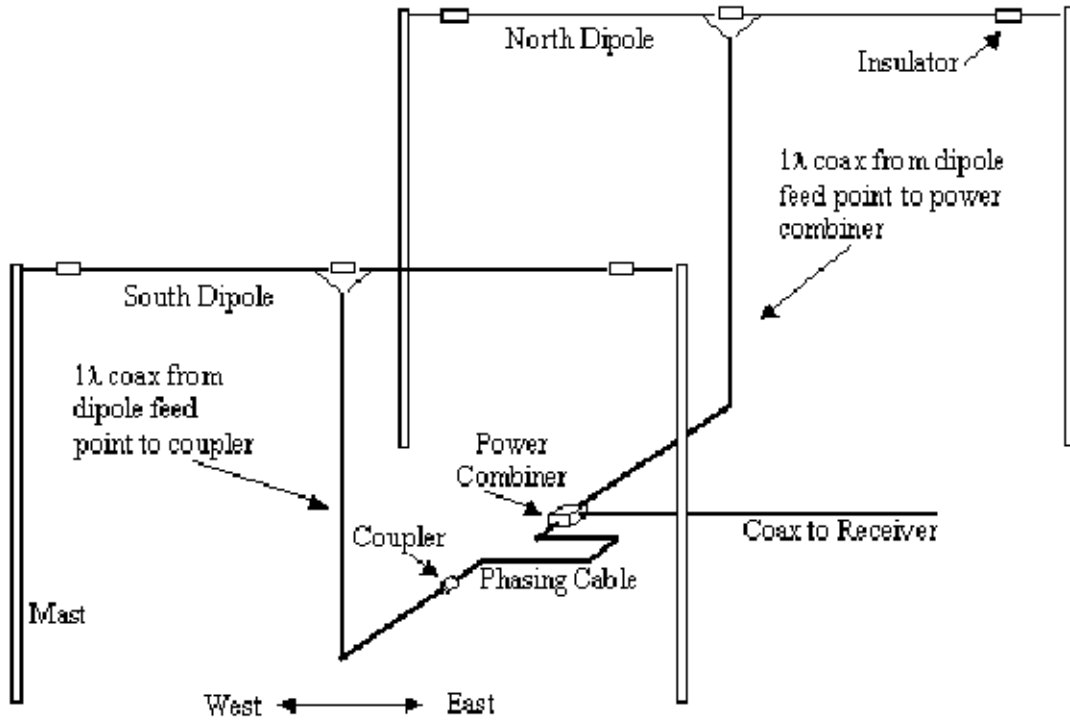


Fig. 9.— Scheme of the two-dipole array (figure from the Jove RJ1.2 Antenna Manual, Dec 2004).

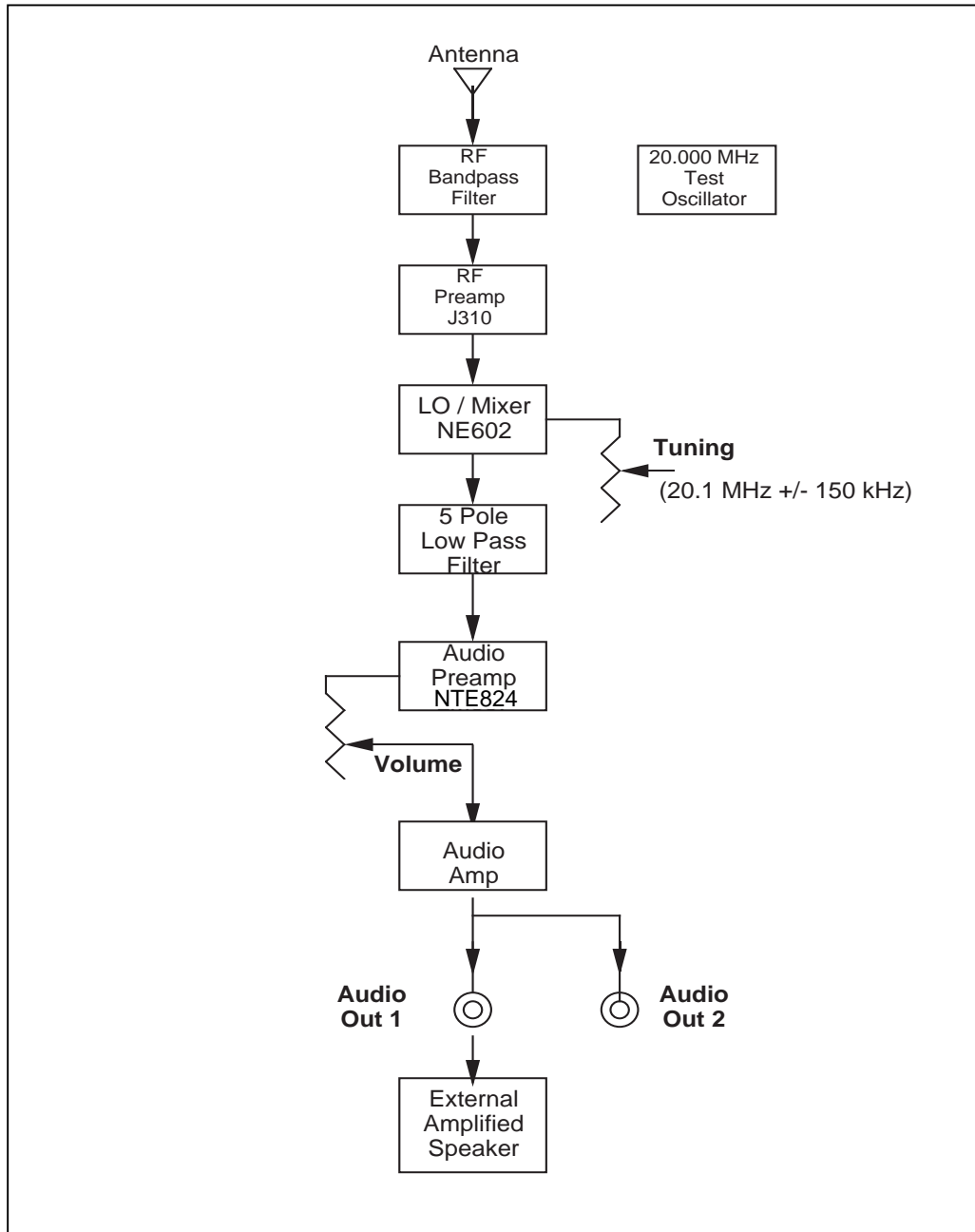


Figure 1. JOVE receiver block diagram

Fig. 10.— Receiver block diagram (figure from the Jove RJ1.1 Receiver Kit Assembly Manual).

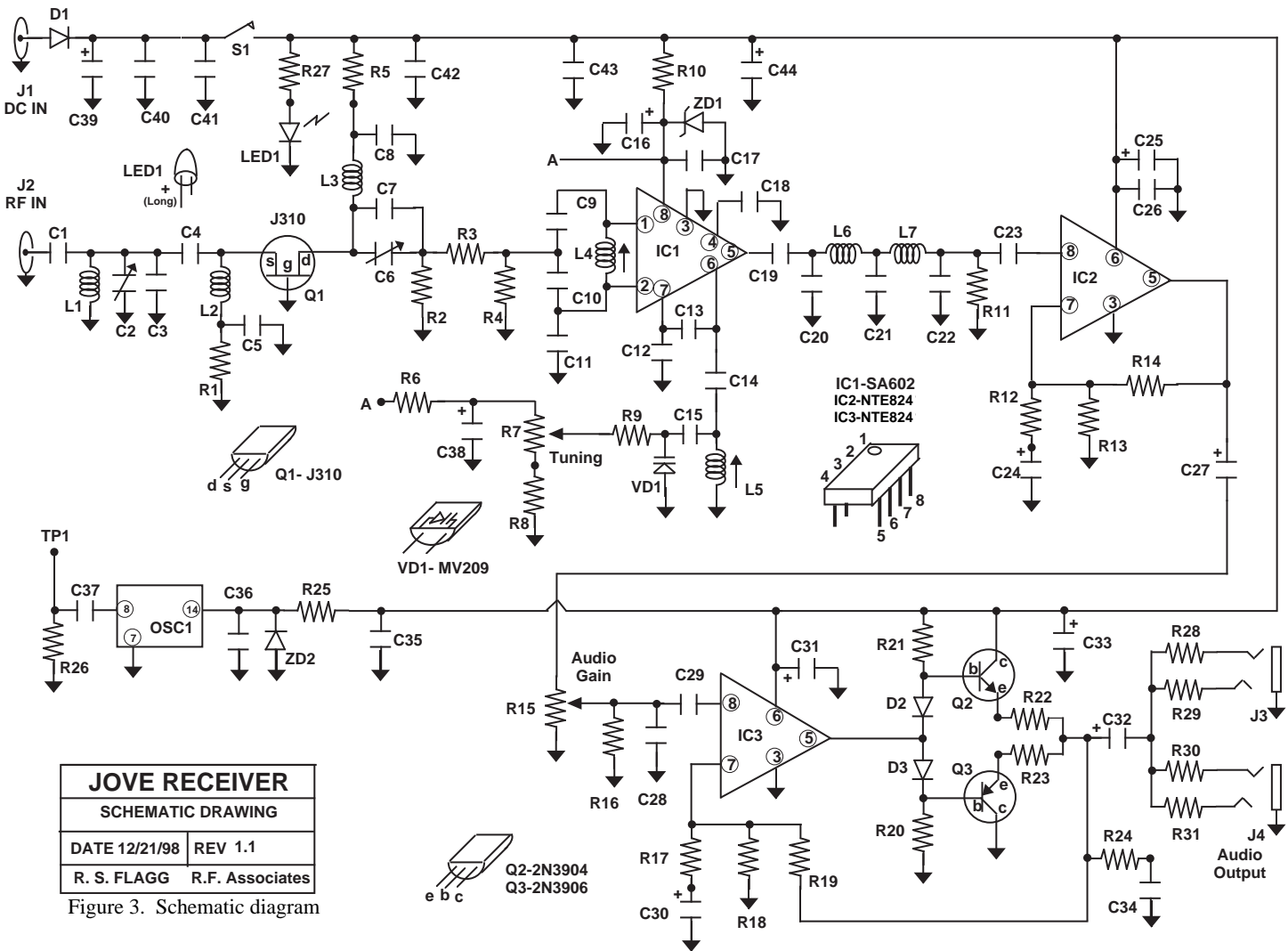


Fig. 11.— Receiver circuit diagram (figure from the Jove R.J1.1 Receiver Kit Assembly Manual).

Fig. 12.— This is a sample power plot and dynamic spectrum recorded using our python based data recorder. The time resolution is 0.1sec, and the frequency scale is in units of 80Hz, so that the entire range corresponds to 8KHz.

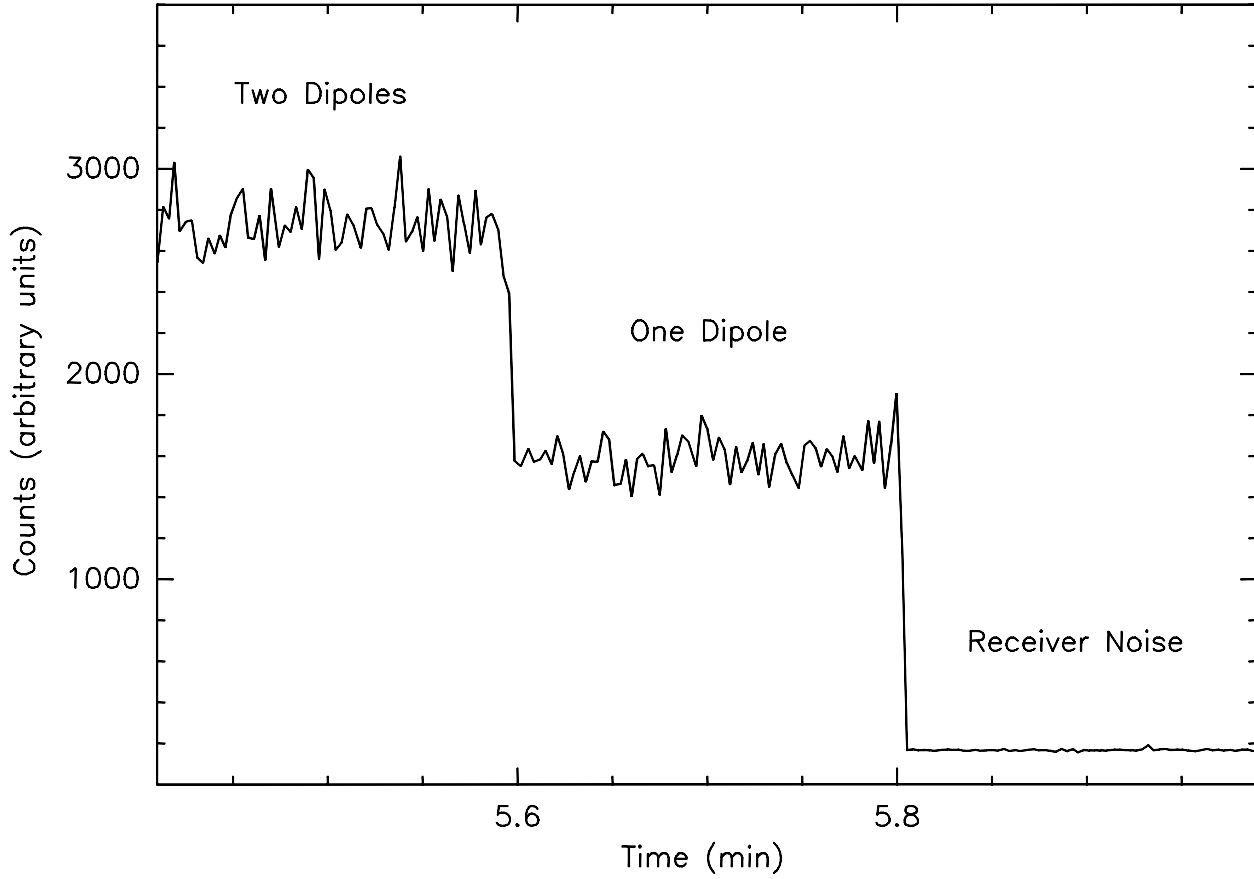


Fig. 13.— Test of the receiver and dipoles. The figure shows the signal detected when two dipoles were connected to the receiver, when only one was, and the receiver noise. Our receiver and dipoles performed as expected, i.e., the receiver noise is less than the natural noise, and the baseline level increased when connecting one and two dipoles.

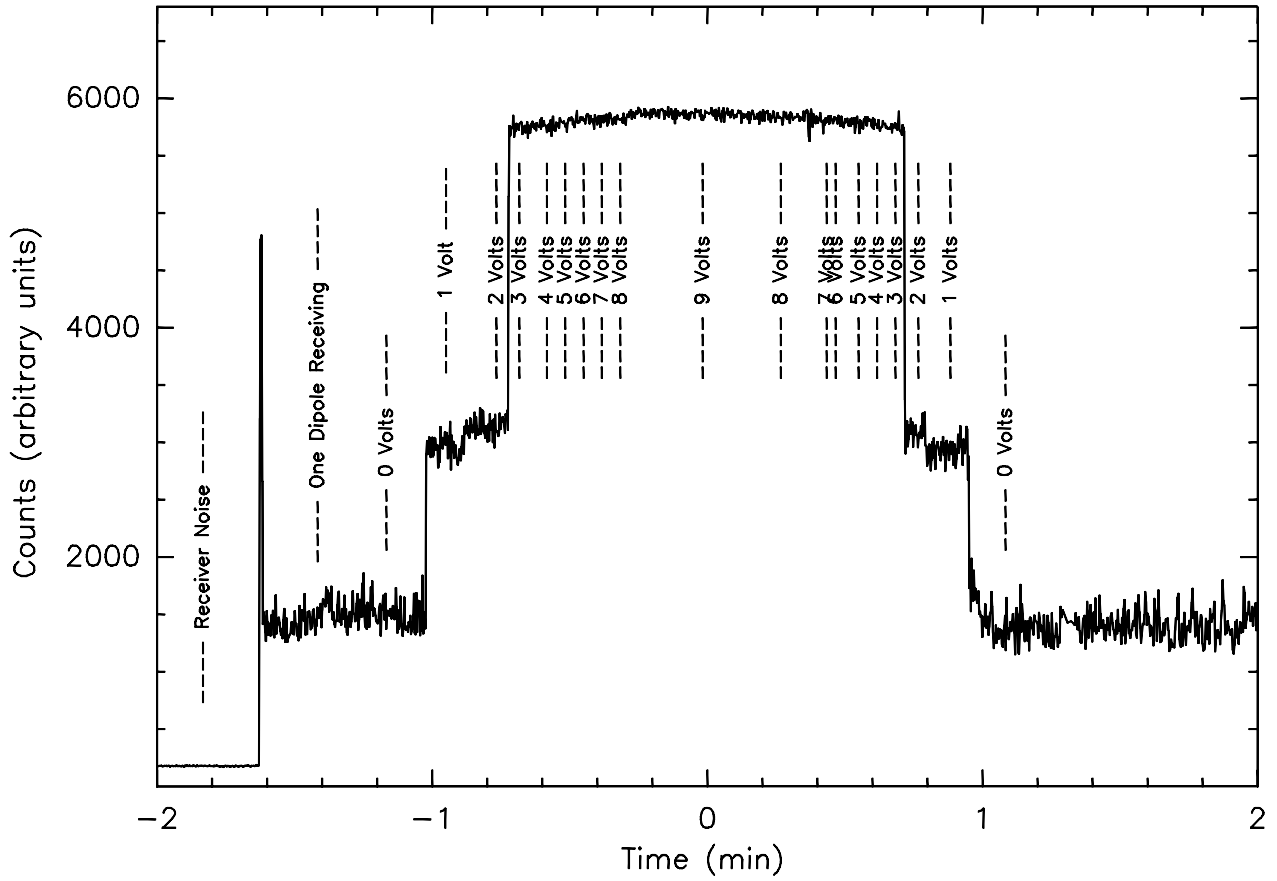


Fig. 14.— Second test of the receiver and dipoles. We connected one of the dipoles to a signal generator and the other to the receiver. We increased the amplitude of the transmitted signal as shown in the figure. This experiment shows that the receiver and dipoles successfully detect external radio signals (in this case a near-field test signal). The apparent saturation is caused by the signal generator and not by the receiver.

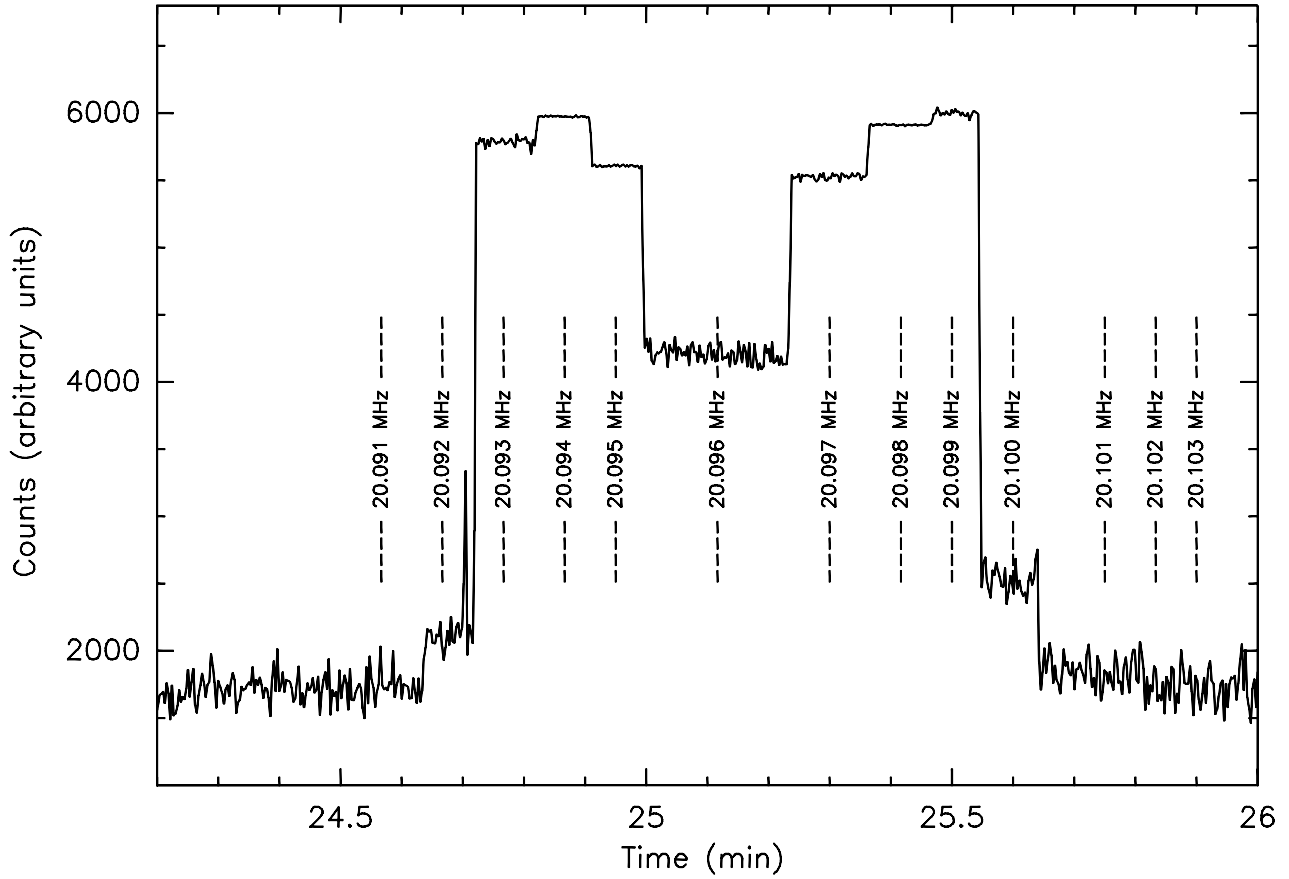


Fig. 15.— Measurement of the receiver bandwidth. We used a tunable signal generator to empirically determine the bandpass shape and bandwidth of our receiver. The test-signal was produced by the signal generator and transmitted by one of the dipoles, while the other dipole was connected to the receiver. The tuning-knob of the receiver was set to the 12 o'clock position. We set the initial transmitted frequency to 20.091 MHz and increased it by steps of 1 kHz as shown in the figure. The bandwidth of the receiver is approximately 7 kHz.

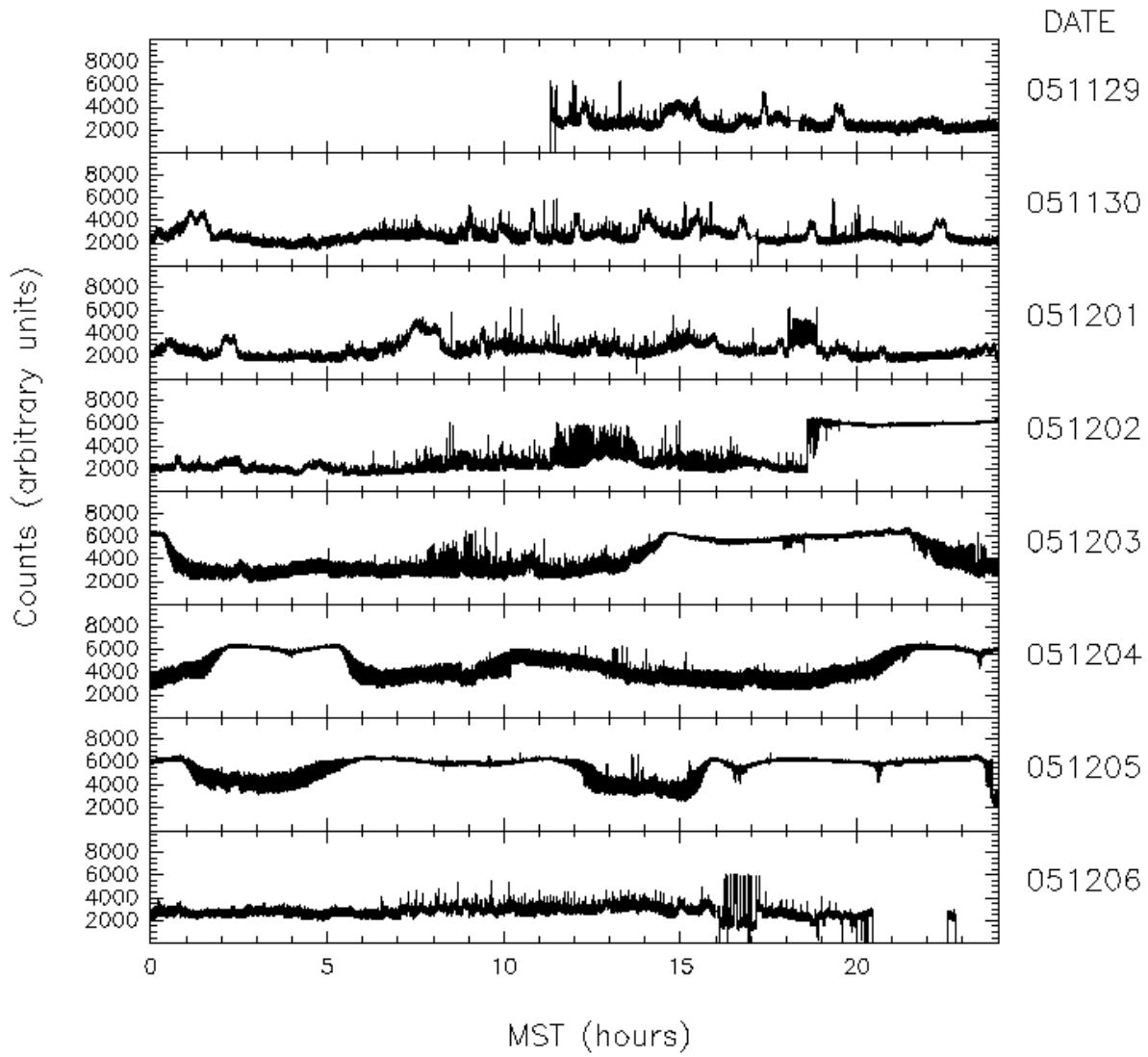


Fig. 16.— Data from the Etscorn observations. We observed approximately 29 days continuously between November 29 to December 27, 2005. The data are shown in counts as a function of local time, for each day independently.

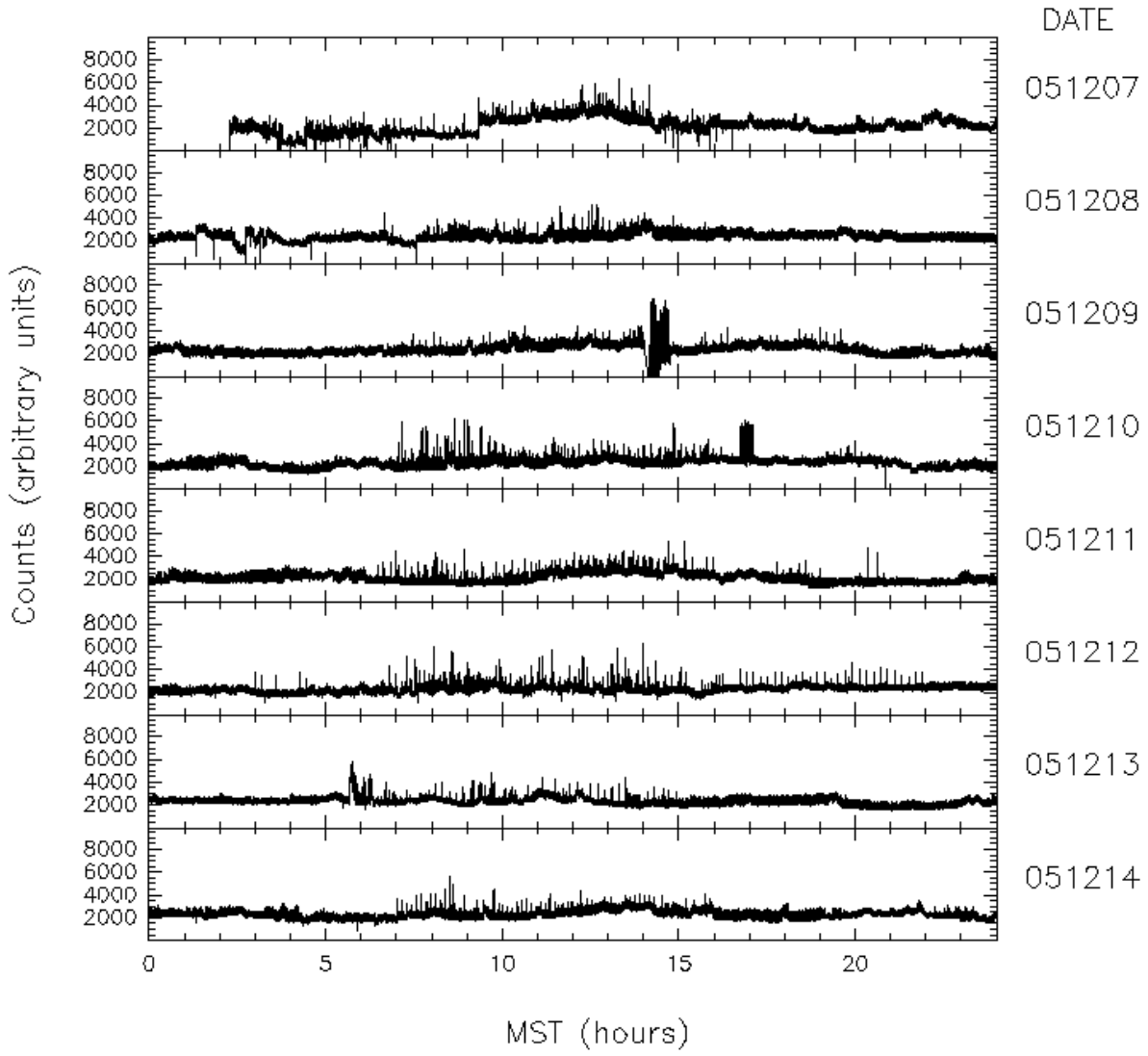


Fig. 16.— cont.

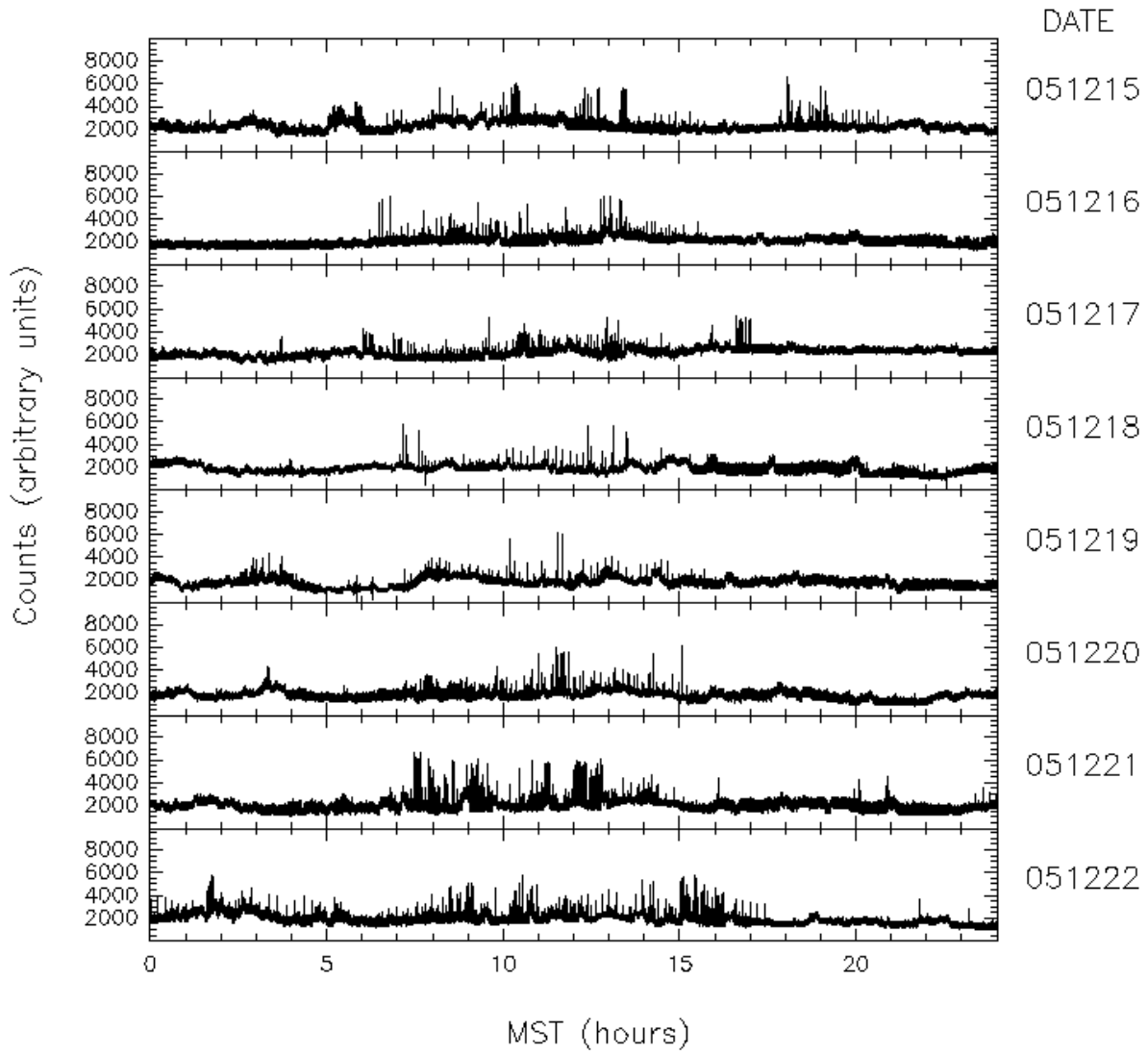


Fig. 16.— cont.

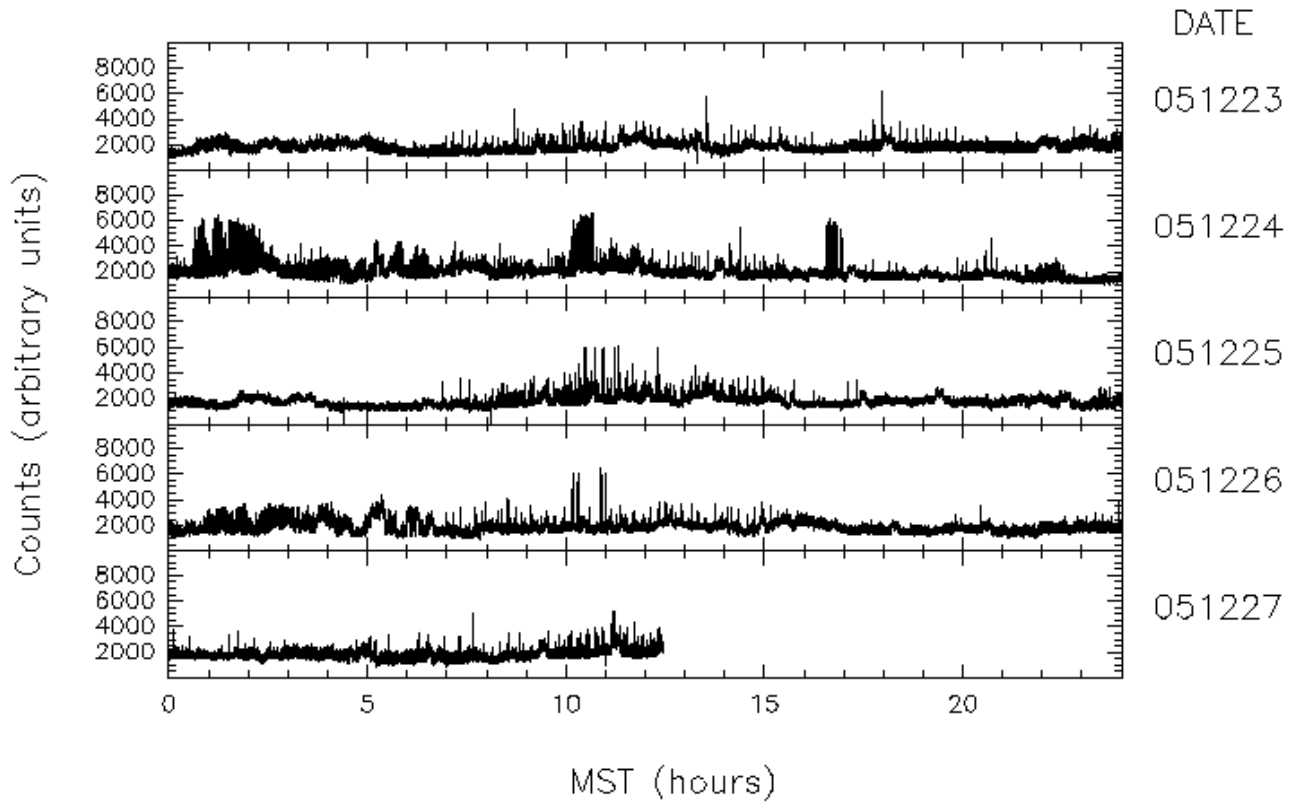


Fig. 16.— cont.

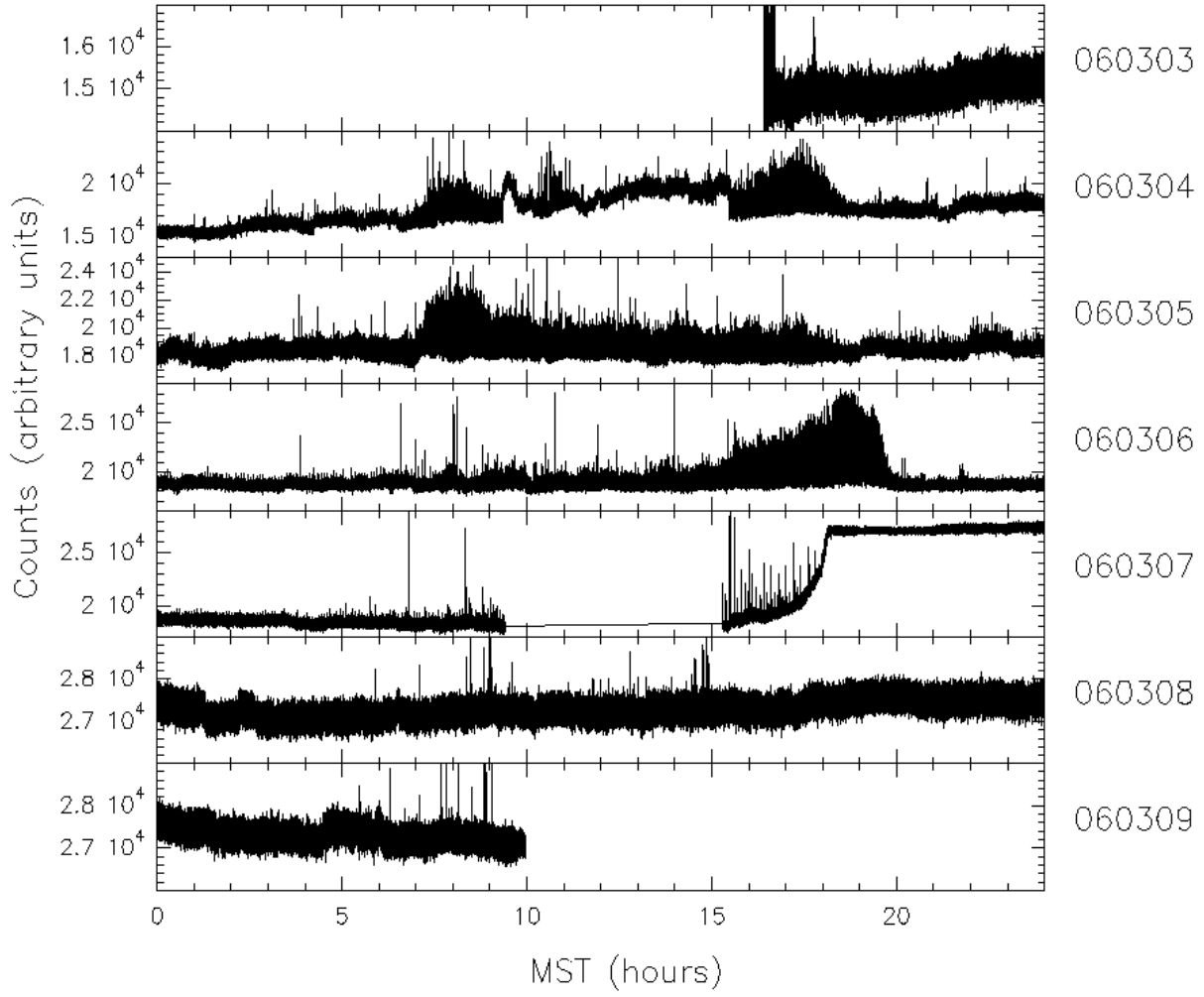


Fig. 17.— Data from the Workman Center observations. The data are shown in counts as a function of local time.

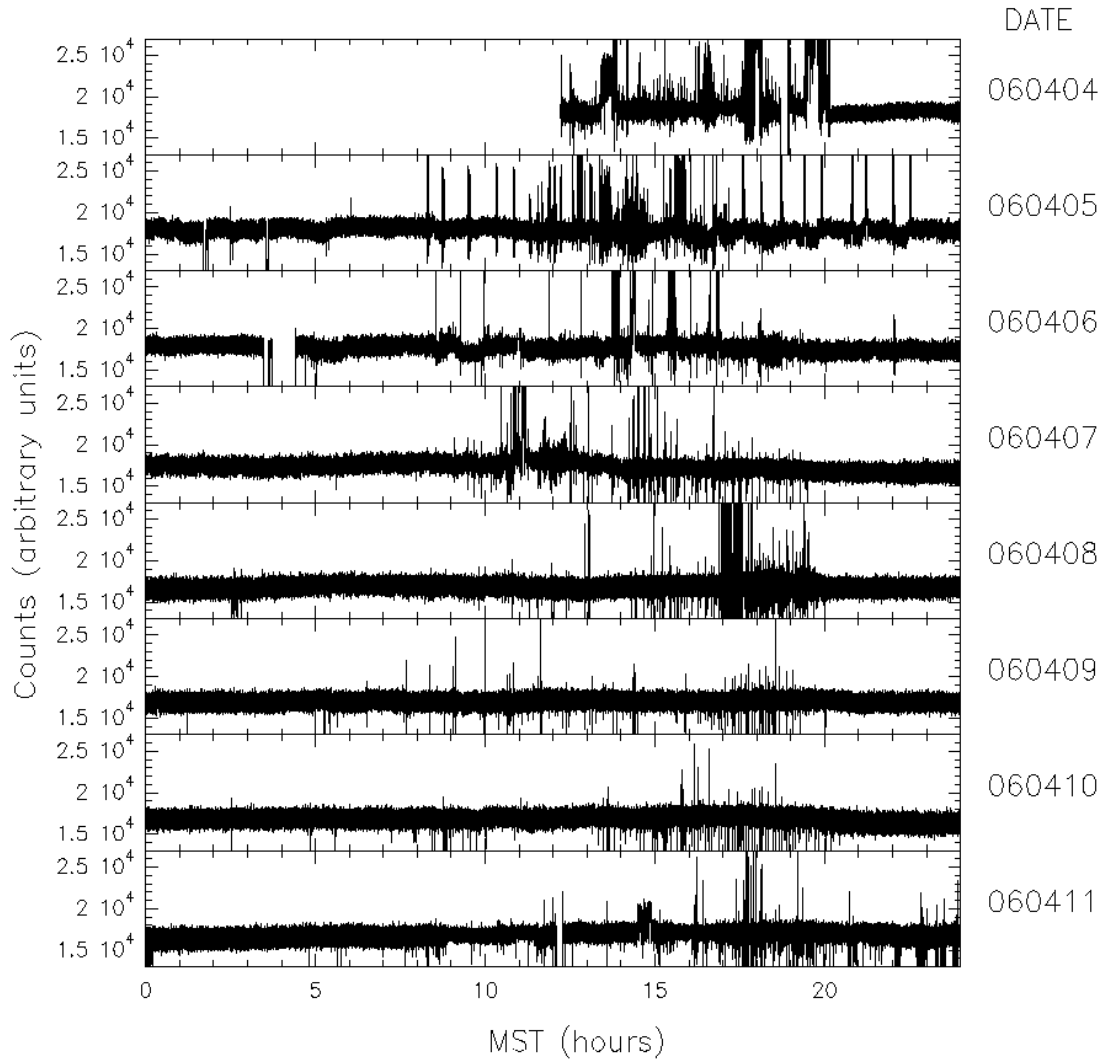


Fig. 17.— cont.

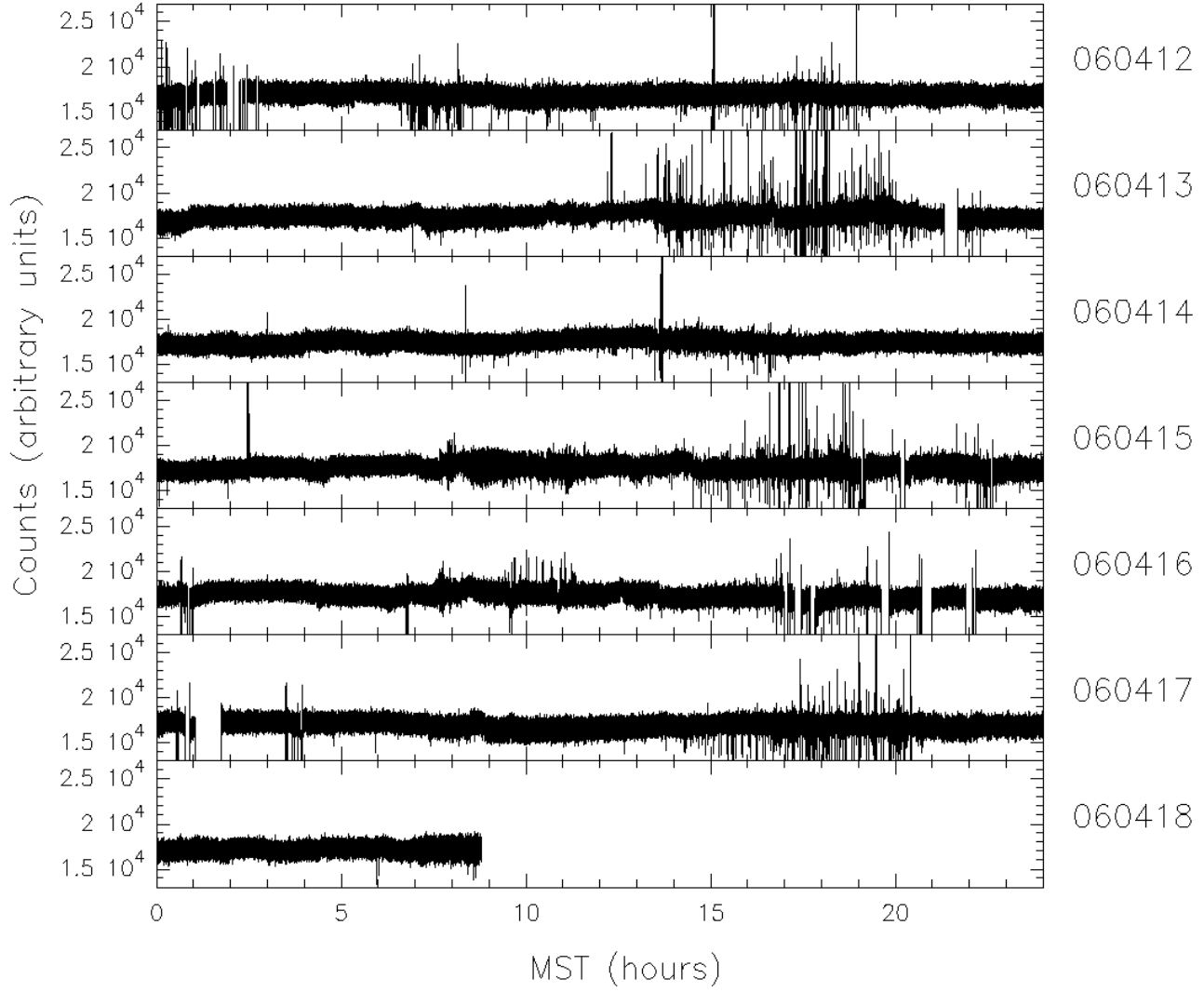


Fig. 17.— cont.

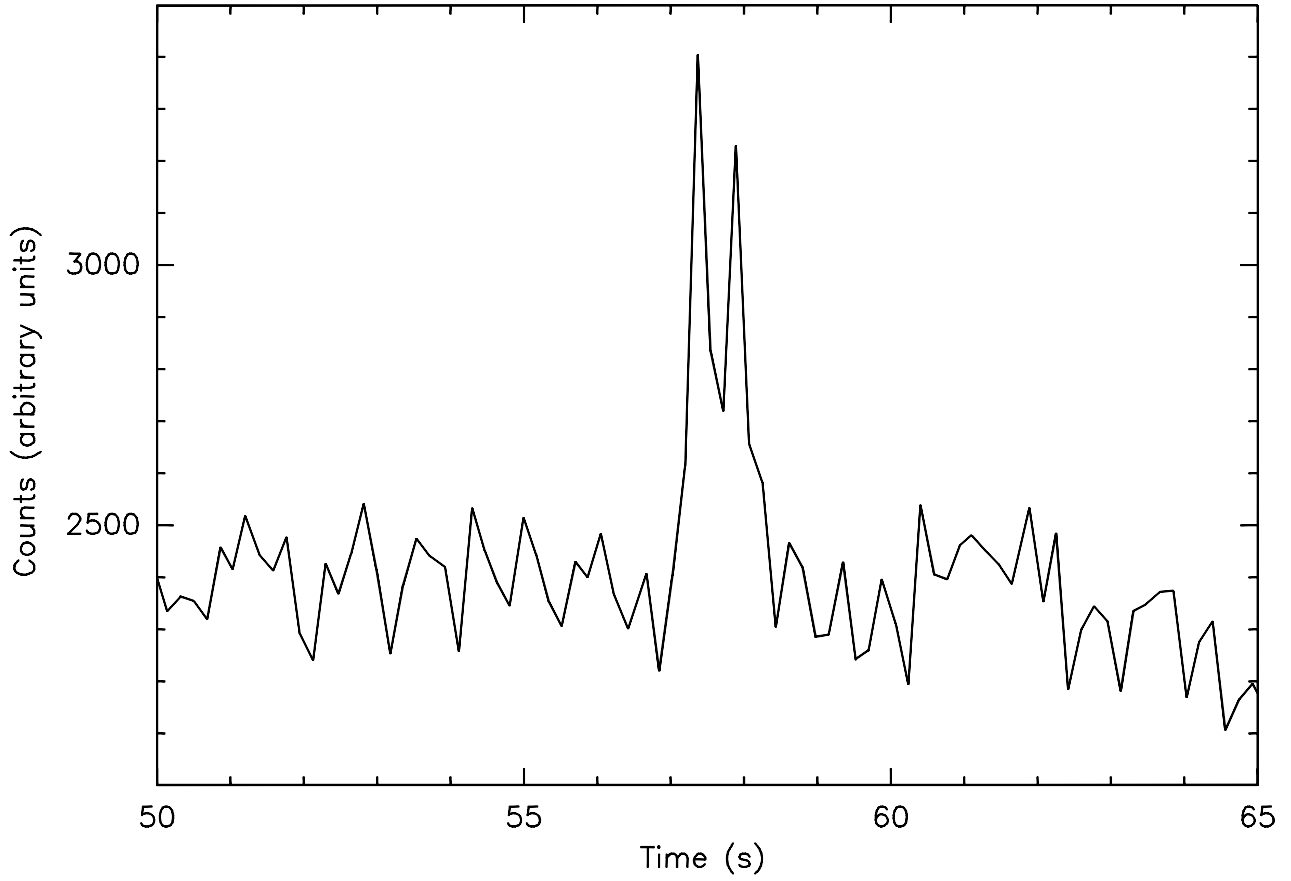


Fig. 18.— Example of a short-RFI event. This kind of short-lasting signals were detected predominantly between 07 and 20 hours MST.

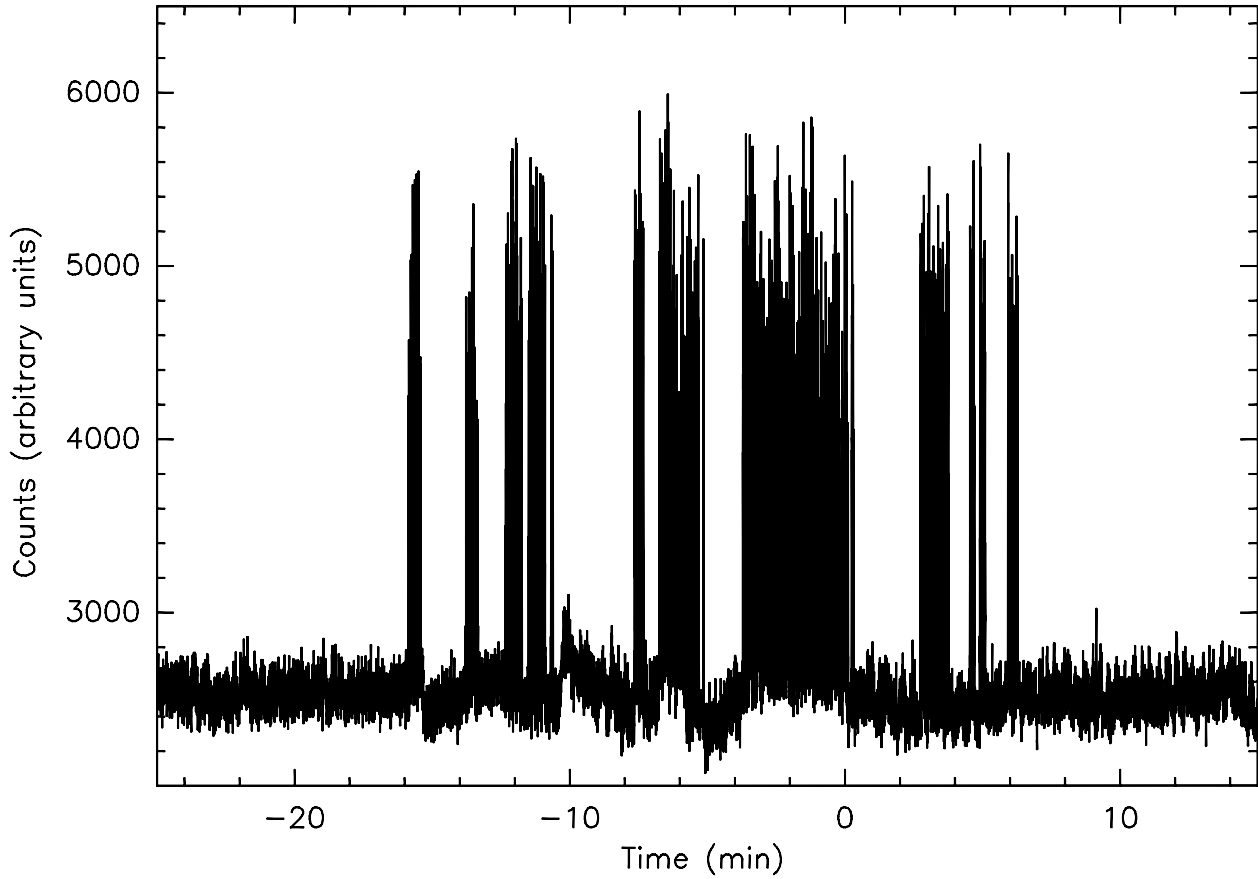


Fig. 19.— Example of a long-RFI event. In this group we classify RFI signals that lasted for several minutes. As exemplified in the figure, this type of RFI could be the superposition of short-RFI events.

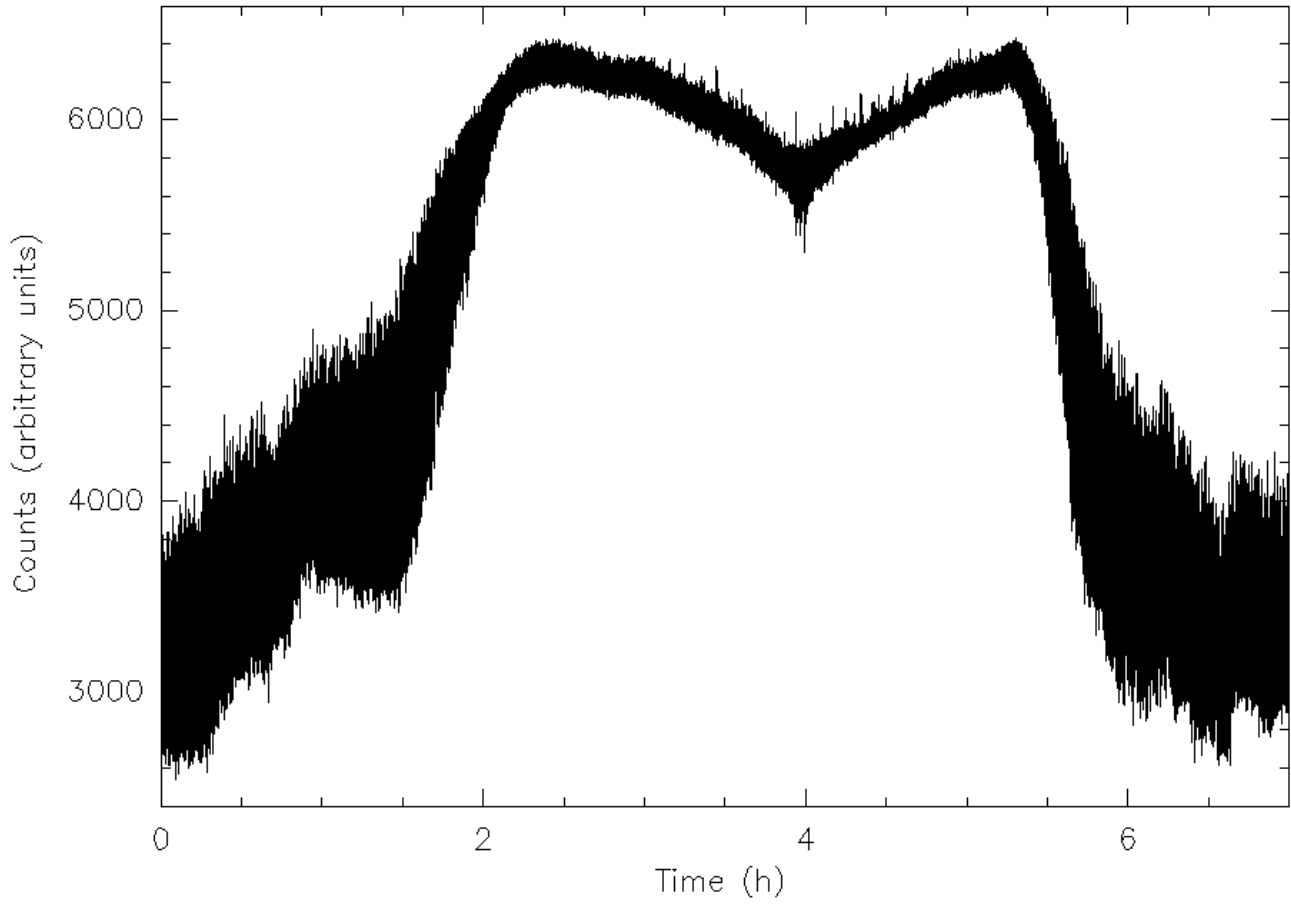


Fig. 20.— Example of a very long-RFI signal. This kind of events lasted for several hours.

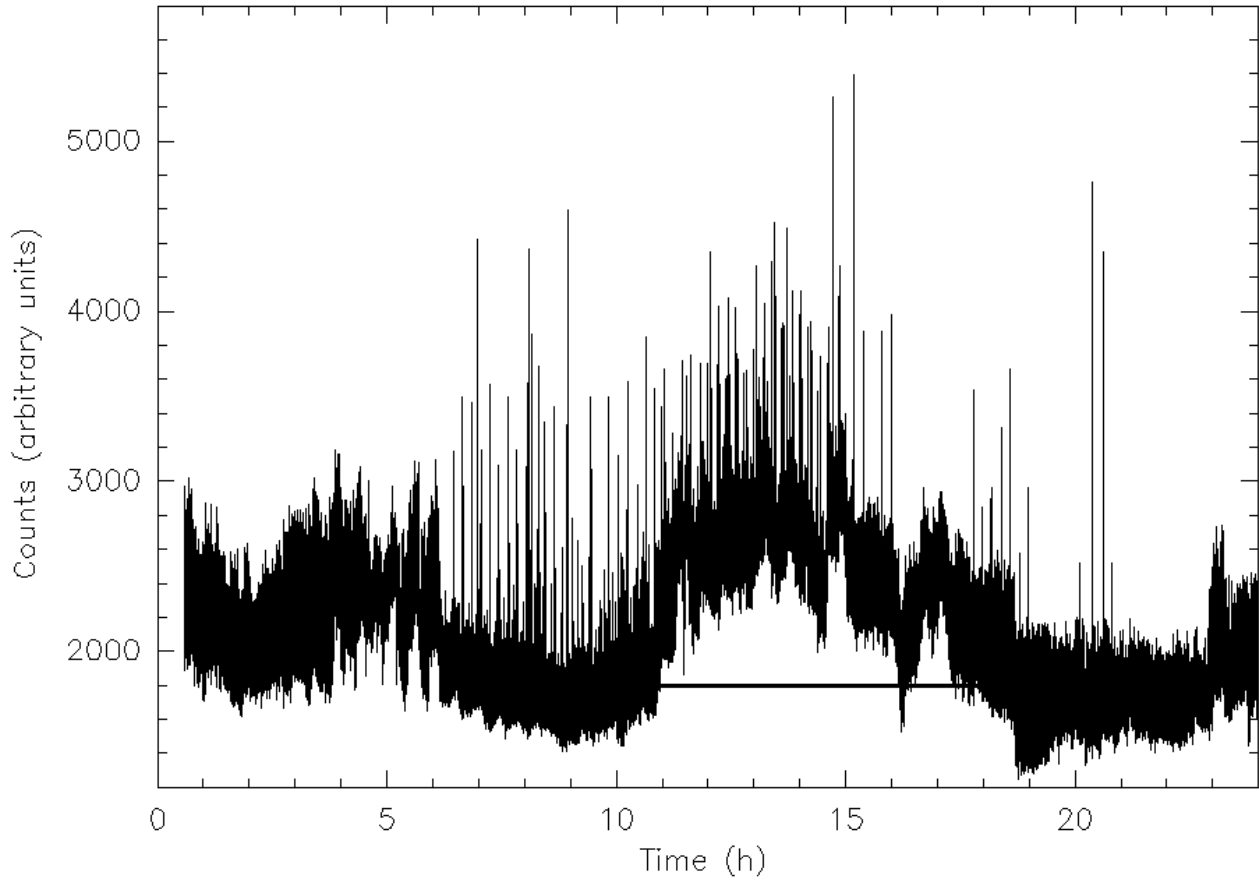


Fig. 21.— Full day of data obtained on December 11, 2005. Note how the bandpass level is systematically higher from 11 to 18 hours MST.

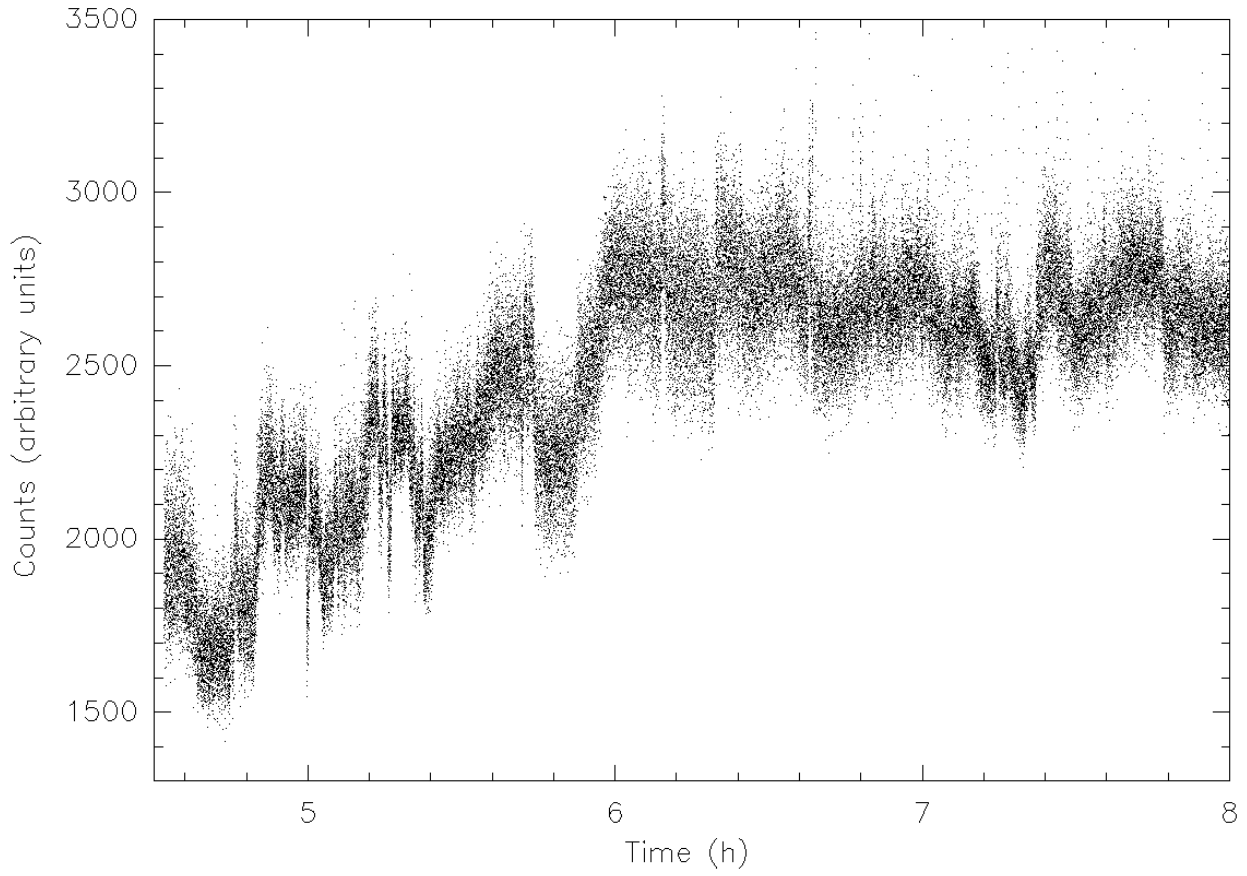


Fig. 22.— Data from November 30, 2005. The time is measure in hours MST. Note the rise in the baseline level at the approximate sunrise time. As a difference of the previous figures, here we show a scatter-point plot of the data to exemplify the density of data points per unit of time recorded in our observations.